THESIS FOR THE DEGREE OF DOCTOR OF PHILOSOPHY

Welding of Ti-6Al-4V:

Influence of welding process and alloy composition on microstructure and properties

Sakari Tolvanen

Department of Industrial and Materials Science
CHALMERS UNIVERSITY OF TECHNOLOGY
Gothenburg, Sweden 2018

Welding of Ti-6Al-4V: Influence of welding process and alloy composition on microstructure and properties

Sakari Tolvanen

ISBN: 978-91-7597-771-3
Series number: 4452
in the series Doktorsavhandlingar vid Chalmers tekniska högskola.
Ny serie (ISSN 0346-718X)

Department of Industrial and Materials Science

Chalmers University of Technology

SE-412 96 Gothenburg

Sweden

Telephone + 46 (0)31-772 1000

Printed by Chalmers Reproservice

Gothenburg, Sweden 2018

To my parents

Welding of Ti-6Al-4V:

Influence of welding process and alloy composition on microstructure and properties

Sakari Tolvanen

Department of Industrial and Materials Science
Chalmers University of Technology

Abstract

Titanium alloys are widely used for components in the fan and compressor sections of aeroengines mainly because of their superior strength-to-weight ratio. Large static compressor components can be manufactured by welding together smaller subcomponents, which has potential to provide benefits such as higher buy-to-fly ratio and improved performance of the components. This is the background for why welding and the mechanical properties of welds have been investigated in this project. The aim of the work was to study what kind of microstructures and defects are formed in welding of Ti-6Al-4V with different welding processes and how these aspects affect the mechanical properties of the welds. Furthermore, the influence of chemical composition of the alloy on the formation of microstructures and defects was studied.

The welding processes compared were electron beam welding, laser beam welding, plasma arc welding and TIG welding. High energy beam welding processes rendered a finer weld microstructure in comparison to the coarser microstructure produced by arc welding processes. The finer weld microstructure was found to be beneficial for tensile ductility and low cycle fatigue performance. Porosity was observed in welds produced by all the processes. Large pores and pores located close to the specimen surface the most detrimental to the fatigue strength. Fatigue life in the welds produced by arc weld processes was more sensitive to porosity than in the high energy beam welds. The finer microstructure has a higher resistance to micro crack initiation and micro crack growth which contributed to the better fatigue performance of welds produced by electron beam welding and laser beam welding.

The alloy composition had a significant influence on the microstructure of the welds and the formation of defects. A small boron addition induced significant grain refinement in the welds in the boron alloyed materials. Narrow columnar prior-β grains were formed in the fusion zones of the boron alloyed welds. The α colonies and α plates were also refined, as compared to the standard Ti-6Al-4V welds. In the cast base material, the TiB particles were located along the prior-β grain boundaries restricting the grain growth in the heat affected zone. In the fusion zone of welds, TiB particles had decreased in size and formed networks of stripes along the interdendritic regions. EBSD combined with prior-β grain reconstruction was an effective method to reveal the prior-β grain structure in the different weld zones. A significant batch-to-batch variation in amount of porosity was observed in laser welding of Ti-6Al-4V. The most significant factors affecting formation of porosity were the material batch, pulse length and welding speed. The material batches that were most susceptible to formation of porosity had increased amount of carbon and oxygen. The formation of porosity could be minimized in all material batches by optimizing the welding parameters.

Keywords: Ti-6Al-4V, welding, defects, porosity, microstructure, fatigue

Preface

The work presented in this thesis was performed at the Department of Industrial and Materials Science (former Department of Materials and Manufacturing Technology) between January 2014 and September 2018. The project has been carried out under the supervision of Professor Uta Klement and Professor Robert Pederson.

The thesis consists of an introductory part followed by the appended papers:

Paper 1 Fatigue strength dependence on microstructure and defects in Ti-6Al-4V welds
Proceedings of the 13th World Conference on Titanium, (2015), pp. 311-315

Paper 2 TIG welding and laser welding of boron alloyed Ti-6Al-4V
Proceedings of the 10th International Conference on Trends in Welding Research, (2016), pp. 321-324

Paper 3 Microstructure and mechanical properties of Ti-6Al-4V welds produced with different processes
Accepted for publication in *Journal of Materials Engineering and Performance*

Paper 4 Microstructure and porosity of laser welds in cast Ti-6Al-4V with addition of boron
Metallurgical and Materials Transactions A, Vol. 49, (2018), pp. 1683-1691

Paper 5 Phase transformation mechanisms in boron alloyed Ti-6Al-4V weld studied using beta grain reconstruction
Manuscript

Paper 6 Batch-to-batch variation in formation of porosity in laser welding of Ti-6Al-4V
Manuscript

Contribution to the appended papers

Paper 1 The author performed the microstructural characterization, fractography and evaluated the results of mechanical testing. Welding experiments and mechanical testing were performed by GKN Aerospace Engine Systems. The author wrote the paper.

Paper 2 The author planned and performed the characterization of the welds and wrote the paper. Welding experiments were performed by GKN Aerospace Engine Systems.

Paper 3 The author performed the microstructural characterization, fractography and evaluated the results of mechanical testing. Welding experiments and mechanical testing were performed by GKN Aerospace Engine Systems. The author wrote the paper.

Paper 4 The author planned and performed the characterization of the welds. Dr. Lionel Germain performed the parent grain reconstruction. X-ray tomography was performed by Dr. Serafina Consuelo and the results were analyzed with help of Mr. Lars Hammar. Mr. Maximilian Haack helped with the quantitative image analysis. Welding experiments were performed by GKN Aerospace Engine Systems. The author wrote the paper.

Paper 5 The author planned and performed the characterization of the weld. Dr. Lionel Germain performed the parent grain reconstruction and helped with data analysis and writing the paper. The author wrote main part of the paper.

Paper 6 The author planned the welding experiments with Mr. Jimmy Johansson. The welding experiments and X-ray radiography were performed by GKN Aerospace Engine Systems. The author performed the material characterization and the data analysis. The author wrote the paper.

Table of contents

1 Introduction

Titanium alloys are widely used for components in the fan and compressor sections of aeroengines owing to their high specific strength and creep properties at moderate temperatures. Large static compressor parts are traditionally manufactured from large single piece castings that are machined into final shape. A significant amount of the initial casting weight is machined away in order to achieve the finished geometry. This is neither environmentally friendly nor economically viable. Fabricating these large static compressor components through welding them out of smaller subcomponents instead of machining them from large single piece castings provides several potential benefits. There will be less scrap material and the structure can be designed to be more efficient owing to the possibility of selecting high strength titanium alloys in specific parts of the structure enabling increased functionality and improved performance, in the end resulting in reduced environmental impact. Fabrication technologies, however, require joining of subcomponents which is why welding and the mechanical properties of welds have been investigated here.

Fusion welding involves localized melting of materials which produces changes and defects in the material, which affect the mechanical properties of weld zones and make the design of fatigue resistant joints a complicated process. The major challenges in welding of titanium alloys are the lowered ductility of weld zones and formation of porosity in the fusion zone. The lowered ductility is attributed to chemical and microstructural changes in the weld zones. There are many reasons for porosity formation in welding which are typically divided into porosity arising from instabilities in the welding process and porosity arising from chemical reactions, evaporation or shrinkage in the meltpool.

Of interest in this study is how the different welding processes and variation in the chemical composition of the base material are influencing the microstructures and defects formed during welding. Welds produced with electron beam welding (EBW), laser beam welding (LBW), tungsten inert gas welding (TIG) and plasma arc welding (PAW) have different microstructures and different populations of defects in terms of their size and distribution. The effect of these aspects on mechanical properties under different mechanical testing conditions have been investigated in the present work. Furthermore, the chemical composition and microstructure of the welded alloy has a significant effect on weldability of a material. The effect of variation in chemical composition of Ti-6Al-4V on formation of porosity in laser welding and the grain refinement effect of boron on microstructure of Ti-6Al-4V welds have been investigated.

1.1 Research Questions

The objective of the work presented in this thesis can be summarized in the following research questions.

- What kind of microstructures are produced with different welding processes?
- How are the mechanical properties affected by different microstructures?
- What size and distribution of defects affect the mechanical properties?
- How is boron addition influencing the microstructure of titanium alloy welds?
- How does variation in base metal composition affect porosity in laser welding of Ti-6Al-4V?

2 Background

2.1 Titanium industry and applications

Titanium alloys have appealing properties which is why they have found applications in a variety of fields. The biocompatibility of titanium makes the material attractive for medical industry, resistance to corrosion makes it appealing for petrochemical and marine applications. Aerospace industry is one of the largest users of titanium alloys where they are used as material for fan and compressor components in jet engines, airframe structures and landing gear in aircrafts, space rockets and satellites. The main reason for the large use of titanium alloys in aerospace industry is their excellent strength-to-weight ratio. Figure 2.1 shows a comparison of specific strength against temperature for several materials. Titanium alloys show the highest specific strength out of most metals up to approximately 500°C [1].

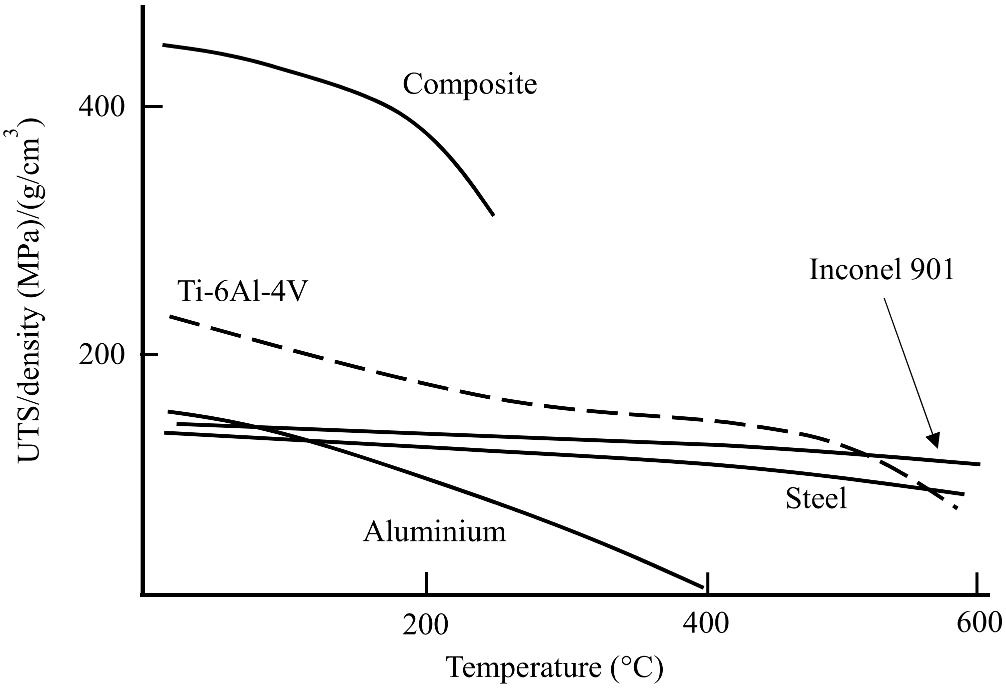

Figure 2.1. A comparison of specific tensile strength (UTS/density) against temperature for various materials. Adapted from [2].

The primary factor limiting more extensive use of titanium is its cost. With a significantly higher cost than aluminum and steel alloys, titanium utilization must be justified for each application. The total cost of titanium stems from high extraction cost from ore to metal as well as high processing costs. Aluminum sheet has the same cost as titanium sponge which needs several additional processing steps to reach the finished product [3]. In addition, machining of titanium alloys is 10-100 times slower than for aluminum alloys [1].

With these factors in mind, much research and development is being devoted to a reduction of the buy-to-fly ratio of titanium components. The buy-to-fly ratio refers to the weight ratio between the initial material and the weight of the final (flying) component after processing and manufacturing. Today, it is still common that up to 90% by weight, or even more, of the initial casting or forging is machined off and turned into scrap. Reduction of the buy-to-fly ratio therefore has high impact and importance on the cost reduction for manufacturing of components. Several technologies are being developed further to reduce the buy-to-fly ratio even more. These include welding, greater use of extrusions, superplastic forming and superplastic forming with diffusion bonding, hot stretch forming to obtain more precise formed shapes, as well as powder metallurgy and additive manufacturing [1].

2.2 Physical metallurgy

Titanium is an allotropic element, which means that it can exist in more than one crystallographic form. At room temperature, pure titanium has a hexagonal close packed (hcp) crystal structure which is referred to as alpha (α) phase. When temperature exceeds 882°C, titanium transforms to a body centered cubic (bcc) crystal structure, called beta (β) phase. The α to β transition temperature, β-transus, is dependent on the alloying elements.

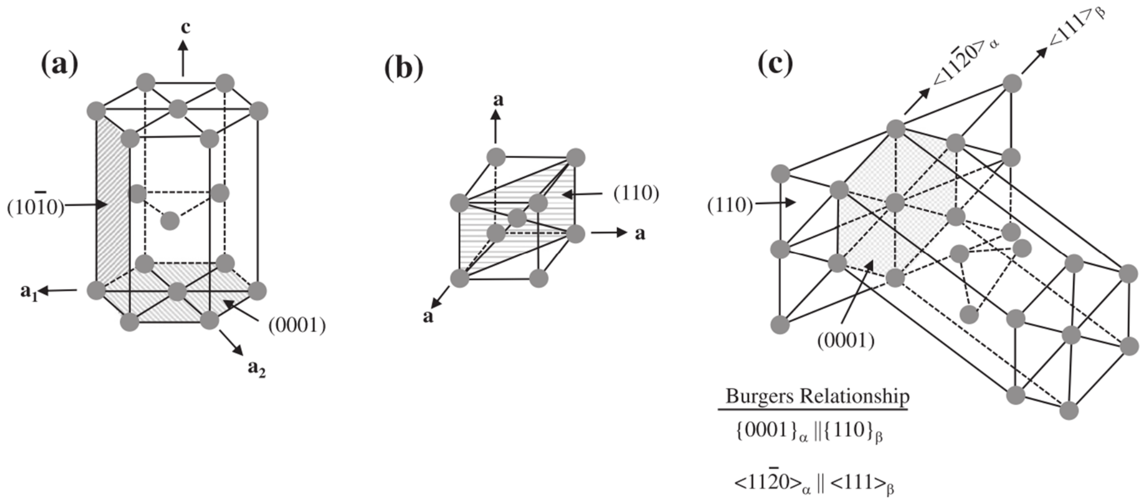

Figure. 2.2. Schematic presentation of crystal structure of a) hcp α phase, b) bcc β phase, and c) the Burgers orientation relationship between the α and β phases. Reprinted from [4], with permission from Elsevier.

The β to α transformation is very important because of its influence on the microstructure formation in titanium alloys. The phase transformation between high temperature β phase and low temperature α phase follows the Burgers orientation relationship (BOR), which is illustrated in Fig 2.2c. According to the BOR the close-packed planes and the nearest-neighbor directions, correspond to each other [5]:

$$\{110\}_\beta // \{0001\}_\alpha \text{ and } <111>_\beta // <11\bar{2}0>_\alpha \qquad (2.1)$$

Depending on cooling rate, the phase transformation can either be diffusionless (martensitic) or diffusion controlled. Both of these transformations occur during welding of titanium alloys and are described in more detail in section 3.2.2.

2.3 Alloy classification

Titanium alloys are alloyed with different elements to achieve improved properties. These alloying elements are divided into i) α stabilizers which elevate the β-transus temperature, ii) β stabilizers which lower the β-transus temperature, or iii) solid solution strengtheners which do not have any significant influence on the β-transus temperature.

The substitutional element Al and the interstitial elements O, N and C are strong α stabilizers. V, Mo, Nb, Ta, Fe, Mn, Cr, Ni, Co, Cu and H are β stabilizing elements. Zr and Sn are considered to be neutral alloying elements and thus do not change the β-transus. The increase in amount of α stabilizers O, N and C leads to a significant strength increase but at the same time decrease the ductility. Titanium has high chemical affinity to these elements, especially at elevated temperature, which is why inert atmosphere needs to be used when processing titanium at high temperatures [6], [7].

Titanium alloys are divided into three main groups, α, α+β and β alloys, depending on which phases dominate at room temperature.

Commercially pure (CP) titanium and α alloys consist of hcp crystal structure at room temperature. CP Ti alloys possess the lowest strength but exhibit best corrosion resistance and also have best weldability. Oxygen and nitrogen are used as alloying elements to increase the strength of CP Ti alloys. α alloys are slightly less corrosion resistant but show higher strength than unalloyed titanium. α alloys cannot be strengthened by heat treatment because they are single phase alloys but on the other hand they offer good weldability. The principal alloying element in α alloys is aluminum, but certain α alloys contain small amounts of β stabilizing elements. Some of these alloys are called near-α alloys and can then be influenced by heat treatment to some degree. α and near-α alloys are characterized also by their high creep resistance which is why they are preferred for use in high-temperature applications [6], [7].

A β alloy is defined as a titanium alloy with sufficient β stabilizer content to suppress the martensitic transformation during quenching to below room temperature. β alloys are metastable, and precipitation of α phase and other phases from the metastable β is a method used to strengthen some of these alloys. β titanium alloys offer the highest strength to weight ratios and very attractive combinations of strength, toughness, and fatigue resistance. They have also good formability due to bcc crystal structure. Some of the disadvantages compared to α+β alloys are increased density, a small processing window, higher cost, and microstructural instability at high temperatures [6], [8].

α+β alloys contain both α and β stabilizing elements. At room temperature equilibrium these alloys usually support a mixture of α and β phases. This makes them the most versatile alloys as the microstructure and mechanical properties of α+β alloys can be modified by adjusting the thermo-mechanical processing parameters. These alloys are used in a wide range of applications from hip replacements to fan blades and airframe structures in aerospace [6], [7]. The Ti-6Al-V alloy studied in this work belongs to the α+β alloys and is the most used titanium alloy.

2.3.1 Ti-6Al-4V alloy

Ti-6Al-4V (Ti-64) is one of the most important titanium alloys. It accounts for about 45% of the total weight of all titanium alloys produced and more than 80% of titanium alloys used in aerospace industry. Ti-64 is also used in medical implants and in automotive, marine and chemical industries. Ti-64 is an α+β alloy which combines attractive mechanical properties with good workability and the best weldability of α+β alloys. This is due to its single-phase mode of solidification which makes it resistant to solidification related cracking. Ti-64 has also low hardenability and the α' martensite in Ti-64 is not as hard and brittle as in more heavily β-stabilized alloys. In aeroengines, Ti-64 is normally used to manufacture components in the fan and the compressor sections, where temperatures do not exceed ~350°C [6].

2.3.2 Boron modified Ti-alloys

Small boron additions to titanium alloys refine the solidification microstructure and α-colony size dramatically. These microstructural refinements improve mechanical properties such as yield strength, ultimate tensile strength, tensile ductility, creep and fatigue behavior [9]–[13].

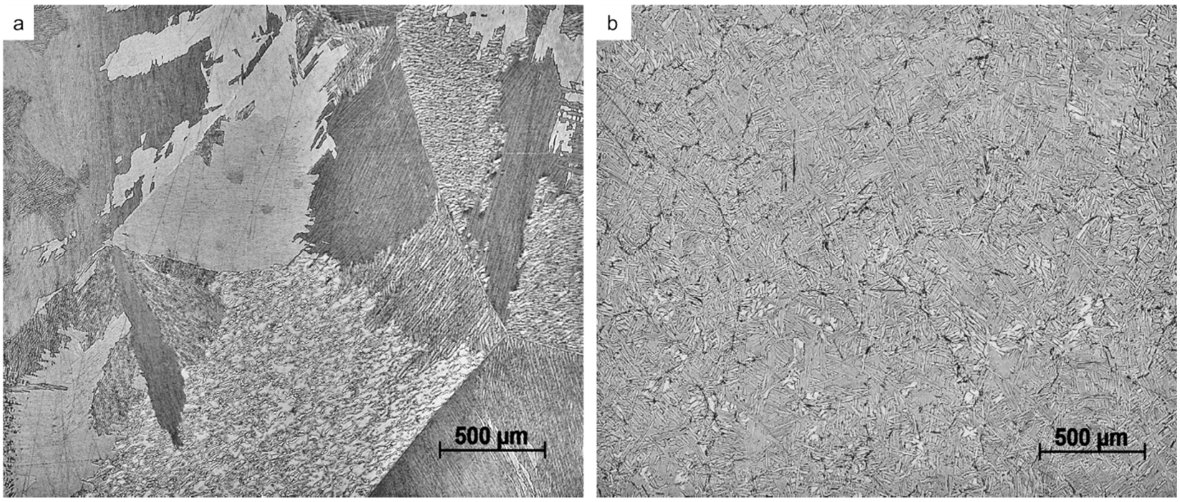

Figure 2.3. Effect of boron on microstructure of cast Ti-64: a) 0 wt-% B and b) 0.11 wt-% B.

Figure 2.3 shows the microstructure of a cast boron-modified Ti-64 alloy in comparison to a standard Ti-64 alloy. As can be seen, the prior β grain size in cast Ti-64 is refined by an order of magnitude by trace addition of boron [9], [13]. Dark areas in prior β grain boundaries of the boron-modified alloy are TiB particles which form via an eutectic reaction in the final stage of solidification. TiB particles also eliminate the grain boundary α layer and refine the α microstructure by acting as nucleation sites for new α plates [12].

The mechanism of how boron refines the prior β grain size is related to its very low solubility in titanium. This causes boron to segregate strongly during solidification which develops a constitutionally super-cooled zone, a boron-rich layer that retards the growth of the solid thereby allowing more nuclei to form in the surrounding supercooled melt, leading to a fine grain size [14]. The degree of grain refinement can be estimated by the growth restriction factor, Q, which describes the influence of solute elements on the grain refinement and characterizes the degree of growth restriction [15].

$$Q = m(k-1)C_0, \quad (2.2)$$

where m is the slope of the liquidus, k, is the partition coefficient (C_S/C_L), and C_0 is the solute content. Solutes that have a high growth restriction factor partition strongly ahead of the solidifying interface and result in a rapid buildup of constitutional supercooling. The fast development of a constitutionally supercooled zone allows the nucleation ahead of an advancing solid–liquid interface and results in a smaller grain size. Boron is one of the most powerful segregating solutes in the titanium system (i.e. boron has a very high Q value) whereas for example aluminum and vanadium provide negligible growth restriction and therefore induce limited constitutional supercooling in Ti–6Al–4V [16].

In cast alloys, boron has been reported to promote formation of equiaxed prior-β grains [17] and that the as cast grain structure changes from columnar to equiaxed at much lower solidification rates than in the absence of boron [18]. The appearance of equiaxed grains in castings implies that constitutional supercooling is more important during solidification than thermal undercooling [13]. In additive manufacturing, formation of fine columnar grains has been reported [14], [19]. The formation of columnar grains is explained by the absence of potent heterogeneous nucleants in the solidification front. However, the columnar structure was significantly refined when boron was added. The lateral rejection of boron during epitaxial nucleation and growth restrict the lateral growth of the dendrites which provides an opportunity for neighboring dendrites to grow [14]. Solidification behavior of metals during welding is further discussed in section 3.2.1.

In titanium alloys with boron, TiB needles are found throughout the microstructures. In cast alloys, TiB particles are mainly located along the prior-β grain boundaries [9], [13], while in additively manufactured and welded alloys TiB particles are typically clustered along the interdendritic regions [14], [20]. This shows that TiB particles do not act as heterogenous nucleation sites for β phase during solidification. The TiB particles are formed during the last phase of solidification via an eutectic reaction. Further, TiB particles formed at the β grain boundaries at the eutectic temperature pin the grain boundary movement and restrict the growth of β grains in the solid state [12].

Microstructural modification by trace boron addition affect also the β to α phase transformation and the morphology of α microconstituents. α phase can nucleate heterogeneously on the TiB particles [12]. A reduction in α colony size, length and aspect ratio of α laths [9], [14], [21] as well as the strength of α texture [12] has been reported.

The microstructural refinement together with the presence of hard TiB particles results in improved mechanical properties. Improvements have been reported on yield strength and ultimate tensile strength [9], [14], [22], [23], ductility [14], [22], [23], fatigue [10], creep [11], and wear resistance [24]. However, addition of higher amounts of boron (> 0.1 wt-% B) increases the volume fraction of TiB particles, which eventually has been shown to act as crack initiation sites during fatigue loading, and can reduce ductility of the alloy [13], [25].

3 Welding of Ti-alloys

For successful welding of titanium and its alloys, several factors need to be considered. Titanium alloys are extremely reactive at high temperatures, particularly in a molten state, and readily pick up atmospheric gases, dirt, grease, and refractories leading to embrittlement of the weld pool. Titanium reacts with elements such as C, O, N, and H, which strengthen titanium but also impair ductility and toughness of titanium welds. The effects of the heating and cooling cycles involved in welding and the influence of alloy composition on the weld microstructure as well as formation of defects need to be considered [6].

3.1 Welding processes

Titanium alloys are readily joined with several common fusion welding processes such as tungsten inert gas welding (TIG), plasma arc welding (PAW), electron beam welding (EBW), and laser beam welding (EBW). Fusion welding processes can be characterized generally by the heat-source intensity. Figure 3.1 illustrates the different characteristics of the aforementioned welding processes and how they affect the penetration.

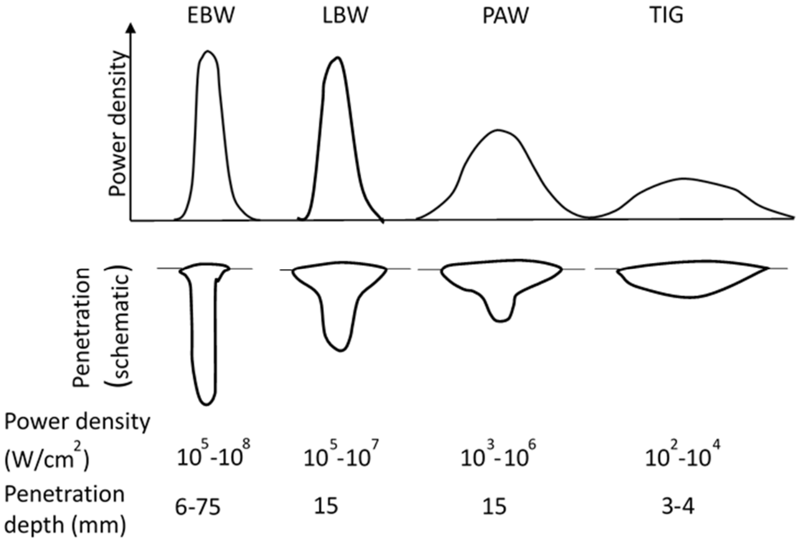

Figure 3.1. Spectrum of practical heat intensities used for fusion welding and its effect on penetration depth. Adapted from [26], [27].

The major advantage of high energy beam welding techniques is the ability to produce welds that are deeper and narrower than by arc welding. Also a much lower heat input is used than what is required in arc welding. The lower heat input results in a narrow fusion zone and heat affected zone and noticeably smaller thermal effects on the workpiece leading to smaller residual stresses and distortions.

3.1.1 Tungsten inert gas welding

Tungsten inert gas welding (TIG) or gas tungsten arc welding (GTAW) refers to an arc welding process using an arc between a non-consumable tungsten electrode and the workpiece. The electric arc is produced by the passing of current through conductive ionized shielding gas. Shielding gas is fed through the torch to provide an inert atmosphere that protects the electrode and the weld pool while the weld metal is solidifying. Argon, helium and their mixtures are used as shielding gases. TIG can be used to produce welds autogenously or a filler material, usually a wire, can be added to the weld pool to fill the joint. The TIG welding process is illustrated in Fig. 3.2.

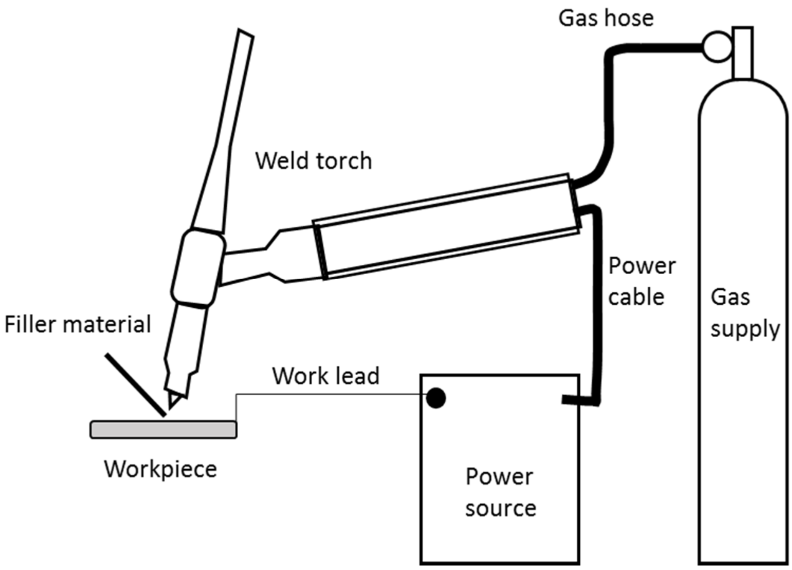

Figure 3.2. Schematic illustration of typical TIG equipment. Adapted from [26].

TIG is a flexible process that can be used to produce welds in many otherwise difficult to weld metals such as magnesium, aluminum, titanium, stainless steels and nickel-based superalloys. TIG is best suited for welding relatively thin sections up to approximately 3-4 mm. For thicker sections multipass welding is required [26]. TIG can be used manually or automated, with or without filler wire. The heat source and filler metal additions can be controlled independently. Welds are generally of high quality, spatter-free, include few defects and there is no slag, hence no post weld cleaning is required. A further advantage is the relatively low cost of the equipment, compared with for example laser or electron beam welding.

The limitations of TIG include the relatively low welding speed and deposition rate which makes it inefficient to weld thick sections. TIG has low tolerance for contaminants in filler and base material and magnetic fields leading to deflection of the arc can make the process difficult to control. Also, the heat input during TIG welding is relatively high.

The main process parameters in TIG welding are arc voltage, welding current, travel speed, wire feed and shielding gas. The amount of energy produced by the arc is proportional to the current and voltage. The amount of energy transferred per unit length is inversely proportional to the travel speed. Helium as a shielding gas produces a hotter arc and deeper penetration than argon. An alternating welding current can be used for better oxide removal and improving welding characteristics. Pulsing of the welding current can be used to control heat input and increase penetration [26], [28].

3.1.2 Plasma arc welding

Plasma arc welding (PAW) is an arc welding process which uses a constricted arc between a non-consumable electrode and the workpiece (transferred arc mode) or between the electrode and the nozzle (no transferred arc mode). Two separate gas flows are used in PAW; plasma gas which flows through the orifice and becomes ionized and shielding gas which flows through the outer nozzle. Usually these gases are the same. Helium, argon and their mixtures are used as shielding gases. Hydrogen and nitrogen may also be added in the mixture. PAW is essentially an extension of the TIG welding process and the differences between the processes are illustrated in Fig. 3.3. TIG uses an open arc while in PAW, the electrode and arc are surrounded by a gas chamber. The plasma gas in the orifice gets heated and ionized which creates a narrow, constricted arc that provides excellent directional control and produces a more favorable depth-to-width weld profile [28].

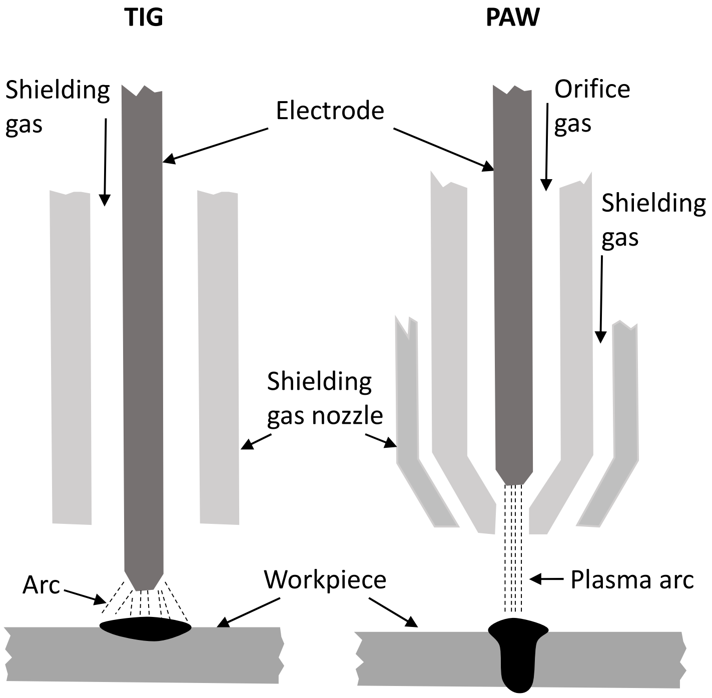

Figure 3.3. The plasma arc is confined in PAW which makes it straighter and more concentrated. Adapted from [28].

PAW can be used in two distinct operating modes, the melt-in mode and the keyhole mode. At lower arc currents, the process resembles TIG and produces a similar weld pool. This melt-in mode is used for material thicknesses below 3 mm. At higher arc currents and plasma gas flow rate, the plasma column can displace the molten metal and form a keyhole. Keyhole mode welding is used for single pass butt welds on material thicknesses from 2.4 mm to 15 mm. Compared to laser welding and electron beam welding, keyhole PAW is more cost effective and more tolerant of joint preparation, though the energy density is lower and the keyhole is wider in PAW [29].

The advantages of PAW compared to TIG include:

- High welding speed: up to 5 times higher than conventional TIG
- Reliable arc ignition and concentrated stable arc with little sensitivity to arc length variation
- Lower heat input leading to smaller heat affected zone and little distortion as compared with TIG welding
- Ability to perform keyhole welding and melt-in-mode welding with the same equipment
- Possibility to weld very thin materials (0.1 mm) and thick materials (15 mm) with a single pass without filler material
- High metallurgical quality in comparison to conventional TIG [28], [29].

PAW can be used to weld the same materials as TIG. Keyhole plasma welding is extensively used to weld stainless steel pipes and tanks. In aerospace industry, PAW is used for airframe components, fuel vessels and gas turbine components. The higher capital cost and complexity of PAW equipment are why PAW has not become more common [28].

3.1.3 Electron beam welding

Electron beam welding (EBW) is a high energy beam welding process, which uses a focused beam of electrons to melt the workpiece surface and create the joint. A high intensity beam of high velocity electrons are concentrated onto a small area. Power densities as high as 10^8 W/cm^2 can be achieved. The high power density can lead to keyhole formation which distinguishes EBW and other high energy density processes from other welding methods.

EBW has the following characteristics in comparison to other weld methods:

- ` High power density of about 10^8 W/cm^2 with a focused beam. A comparison with other welding processes is shown in Fig. 3.1
- High welding speed for welds with high depth-to-width ratio, small heat affected zones and little distortion
- Production of welds with very shallow to very deep penetrations
- The welding process is carried out in vacuum which provides good protection of the weld pool against contamination.

The capital cost of EBW equipment is a major drawback in comparison to conventional welding processes. The cost of joint preparation and tooling is also higher because the small electron beam spot size requires a precise joint gap. The vacuum chamber limits the size of the workpiece and the production rate is affected by the need to evacuate the chamber for each production batch [26], [30].

3.1.4 Laser beam welding

Laser beam welding (LBW) uses a concentrated laser beam as the source of heat. The coherent nature of the laser beam allows it to be focused to a small spot which allows narrow and deep welds with high welding speeds.

The first laser was introduced in 1960 but its use for welding application was limited until the introduction of high-power continuous-wave lasers in the 1970s. High-power continuous-wave lasers include CO_2, Nd:YAG, fiber, disk and most recently high-power diode lasers. A comparison of properties between different types of lasers is shown in Table 3.1.

Table 3.1. Properties of high-power lasers [27].

	Wavelength [µm]	Average continuous power [kW]	Beam quality
CO_2	10.6	50 max, 1-15 normal	Average-Good
Nd:YAG	1.06	10 – 15	Poor
Fiber	1.07	100	Good
Disk	1.03	16	Good
Diode	0.98	10-15	Poor

CO_2 lasers were the first high-power lasers used for welding applications. Until recently CO_2 lasers have offered the highest output power, good beam quality and relatively low machine cost making them an attractive alternative especially for welding thick sections. CO_2 lasers operate at 10.6 µm wavelength which causes most of the disadvantages related to CO_2 lasers. Common transparent materials such as glass and quartz are opaque to 10.6 µm wavelength laser radiation which makes it impossible to use optical fiber systems. This limits the flexibility of CO_2 laser systems. The 10.6 µm wavelength has also lower absorptivity on metals and higher absorptivity on laser induced plasma [27].

Solid state lasers operating at wavelengths close to 1 µm have a benefit that the laser radiation can be delivered via optical fiber which makes the laser systems more flexible. The 1 µm wavelength has higher absorptivity on metals and lower absorptivity on the plasma. Early high-power solid state lasers, Nd:YAG lasers, had relatively poor beam quality and electrical efficiency. The development of disk and fiber lasers has improved the beam quality and electrical efficiency significantly. Direct diode lasers are the latest development. They have excellent electrical efficiency and compact size but poor beam quality allows only conduction mode welding [27].

Laser beam welding has numerous benefits over traditional welding methods. However, it has also several limitations that need to be considered.

Major advantages of LBW include:

- Focused laser light provides high energy density
- High processing speed and narrow welds with deep penetration
- Heat input is close to the minimum required to fuse weld metal. Distortions and metallurgical effects in heat affected zone are minimized
- Can be used under ambient atmosphere or shielding gas. No vacuum required
- No electrodes or filler materials required
- Difficult-to-weld materials, such as titanium and glass, can be joined
- Can be used in keyhole mode or conduction mode
- Can be readily mechanized for automated high-speed welding
- The laser beam can be transmitted to several workstations using beam-switching optics.

Limitations of LBW include:

- Laser welding equipment is almost 10 times more expensive than a comparable arc welding system although they are cheaper than EBW systems and have higher productivity than conventional arc welding
- Joints must be accurately positioned because of the small size of the laser beam
- Maximum joint thickness is limited compared to EBW
- The high reflectivity and high thermal conductivity can affect laser weldability of some materials [26], [27], [30].

3.1.4.1 Laser welding fundamentals

Absorption of the laser light occurs when the incident beam hits the surface of a solid metal. The absorption occurs via Fresnel absorption, where the incident light is partially absorbed and partially reflected by an opaque surface. Absorption of the laser light is dependent on the substrate properties, as well as the characteristics of the incident laser light. For example, titanium at room temperature has an absorptivity of 0.4-0.5 for light with 1 μm wavelength (solid state lasers) and <0.1 for 10 μm wavelength (CO_2 laser) [31]. The absorptivity increases significantly at the melting point of the material. At beam intensity below 10^4 W/cm^2, welding occurs in so called conduction mode. Transition to keyhole laser welding occurs at about 10^4-10^6 W/cm^2 due to the vaporization of metal. The intense vaporization distinguishes keyhole laser welding from other conventional joining methods. It causes a large increase in vapor pressure (recoil pressure) that drills a depression in the melted metal, forming a long and narrow cavity called a keyhole which is illustrated in Fig. 3.4. The laser beam can then penetrate deeper into the metal through the cavity. As the beam reaches the keyhole surface, beam energy is partially absorbed on the surface and partially reflected towards a new point of interaction. This multiple reflection Fresnel absorption increases the overall energy absorption up to 90% (or more). The keyhole cavity is filled with metal vapor that partly absorbs the incoming laser light. The charged particles present in the vapor can gain kinetic energy from the beam photons via inverse Bremsstrahlung absorption.

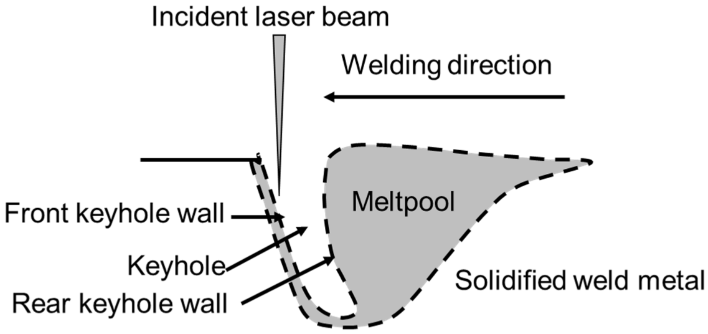

Figure 3.4 Schematic view of a keyhole. Adapted from [32].

During keyhole laser welding the keyhole is formed and kept open by the pressure of the evaporating metal, so called ablation or recoil pressure. The forces that try to close the keyhole are surface tension and hydrostatic pressure. The recoil pressure is also one of the forces driving the flow of molten metal in the meltpool. It causes a downward flow of melt in the front keyhole wall transporting the molten metal around the keyhole. Marangoni force is induced by temperature gradient of surface tension which makes the melt to flow towards the higher surface tension. For most metals the surface tension decreases as a function of temperature. As a result, surface tension gradients, and liquid flow, will exist from center of the meltpool towards the solid-liquid interface [33]. Frictional fluid flow induced by the metal vapor ejected from the keyhole and buoyancy forces are also affecting the meltpool flow [34], [35].

3.2 Welding metallurgy of Ti-64

3.2.1 Solidification

Solidification behavior controls the size and shape of grains in welded microstructures, the extent of segregation, the distribution of inclusions, the extent of defects such as porosity and hot cracks, and ultimately the properties of a solidified weld metal. The solidification behavior is influenced by various parameters such as temperature gradient, growth rate of the solidification front, undercooling as well as the alloy system [36].

When a liquid is cooled below its melting temperature, there is a driving force for solidification. The initial solidification in a weld occurs epitaxially at the meltpool walls. Epitaxial solidification is a heterogenous process. Homogenous nucleation requires high undercooling which does not normally occur in meltpool conditions. After nucleation, growth of the solid occurs by the addition of atoms from the liquid to the solid at the solid/liquid interface. The nature of the solid/liquid interface will be determined by the thermal gradient (G) and the growth rate (R) at the solid/liquid interface. The mode of solidification can be planar, cellular, or dendritic depending on the solidification condition. A solidification map in Fig. 3.5 shows the variation of microstructure as a function of G and R, and the effect of these two variables. Ratio G/R is related to undercooling and the product G*R is related to cooling rate. High G/R ratio will generate a planar mode while a low G/R will generate dendritic solidification. High cooling rate (G*R) will produce finer solidification microstructure than slow cooling rates. The solidification conditions may change during solidification. During welding the ratio G/R decreases from the fusion line toward the centerline. This suggests that the solidification mode may change from planar to cellular, columnar dendritic, and equiaxed dendritic across the fusion zone [36].

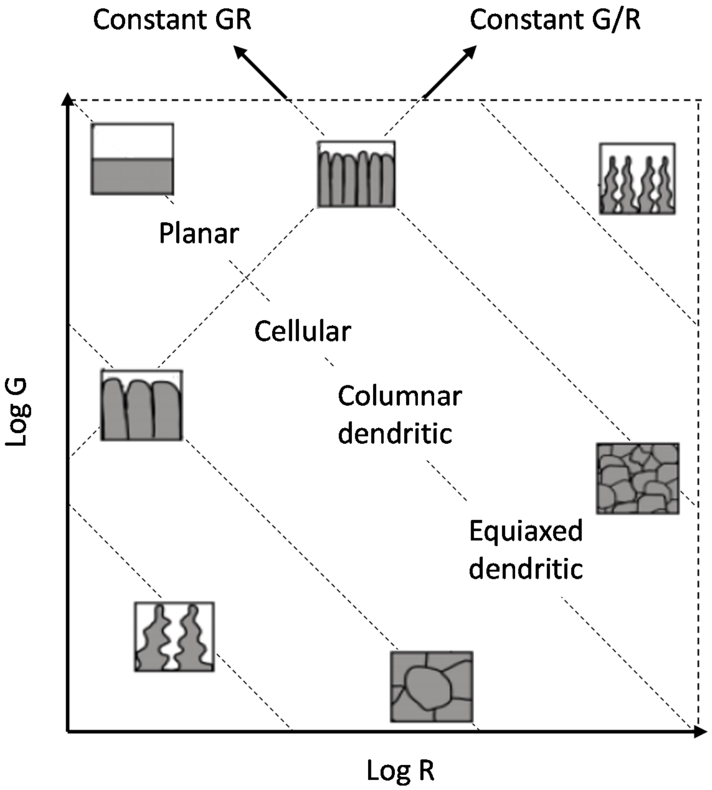

Figure 3.5. Solidification map showing the variation of solidification microstructures as a function of the temperature gradient (G), growth rate (R), and the combinations of these two variables as GR (cooling rate), and G/R undercooling. Adapted from [37], [38].

Constitutional supercooling occurs during solidification of alloys. The solute is partitioned into the liquid ahead of the solidification front. This causes a corresponding variation in the liquidus temperature producing conditions where the melting point of the liquid is higher than the temperature of the liquid. This allows small perturbations on the solid/liquid interface to expand into the supercooled liquid. The tip of any protuberance will be at a higher temperature than the planar front. However, as long as the temperature of the tip is lower than the melting temperature, solidification can occur and the tip may grow in a cellular/dendritic manner. As shown in Fig. 3.6, increasing constitutional supercooling favors dentritic growth.

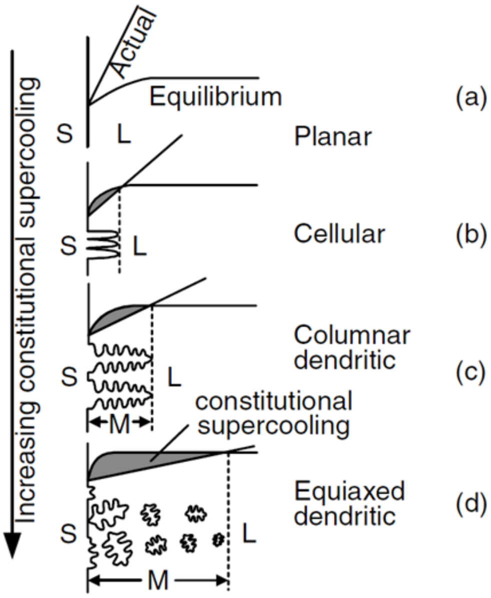

Figure 3.6. Effect of constitutional supercooling on solidification mode [36]. S indicates solid, L liquid and M mushy zone. Reproduced with permission from John Wiley and Sons.

During welding of titanium alloys, β grains nucleate epitaxially and grow preferentially towards the maximum temperature gradient. The favored growth direction for the dendrites in metals with cubic crystal structure is in the <100> direction. Therefore, the nucleation sites with the <100> direction aligned with the temperature gradient will outgrow less favorably oriented grains. Large grains in the base material and the heat affected zone provide fewer epitaxial growth sites at the fusion boundary and dictate large prior β grains in the fusion zone [36], [39], [40]. The absence of segregating elements in Ti-64 also provides limited constitutional undercooling which leads to coarse prior-β grain structures in cast and welded alloys. Therefore, addition of boron as a measure of grain refinement has been investigated recently and its influence is reviewed in more detail in section 2.3.2. Ti-64 has very narrow freezing range, approximately 5°C. Hence, it behaves like a pure metal during solidification. The narrow freezing range and absence of segregating elements and low melting phases makes Ti-64 welds unsusceptible to solidification related cracking which may be a problem for other high strength structural metals [6].

Under two-dimensional heat flow conditions, which is typical for keyhole EBW and LBW, columnar β grains growing from the base material inwards are formed. Under three-dimensional heat flow conditions, typical for TIG, more complex, multidirectional β grain morphologies are formed [6]. The prior-β grain size in the weld zones increases with increasing heat input of the welding process [39], [41].

3.2.2 Continuous cooling

The α+β titanium alloys such as Ti-64 form complex microstructures during continuous cooling from β phase field. Depending on the cooling rate from β phase field, the transformation can be diffusionless (martensitic) or nucleation and diffusion controlled. For high cooling rates the transformation will be diffusionless forming martensite. In titanium alloys two martensite morphologies are observed, massive and acicular martensite. The massive martensite consists of very thin laths (0.1 - 1 µm), which all have similar crystal orientation and can be observed as irregular areas that are hard to resolve with light optical microscope. The acicular martensite consists of individual α laths, each with different crystal orientation [7].

Slower cooling rates lead to a diffusion controlled transformation. The α phase first nucleates preferentially at β grain boundaries forming a continuous α layer along β grain boundaries. During continued cooling, α plates nucleate at the β grain boundaries and grow into the β grains as parallel plates belonging to the same variant of the Burgers relationship forming a so-called α colony. The α colonies continue to grow until they meet another α colony. With increasing cooling rate, the size of the α colonies as well as the thickness of the individual α plates becomes smaller. At higher cooling rates, α plates start to nucleate also at the α colony boundaries and start to grow perpendicular to the nucleation site forming basketweave structure [7].

Ahmed and Rack [42] demonstrated that martensitic, massive and diffusion-controlled phase transformations occur in Ti-64. Cooling rates above 410°C/s are required to achieve fully martensitic microstructure, a massive transformation is observed between 410 and 20°C/s which is gradually replaced by diffusion controlled Widmanstätten α-formation. During a martensitic transformation, the composition of martensite remains the same as that of the parent β phase, but the crystal structure changes from bcc to hcp. The microstructure formed through diffusional transformation is also influenced by the cooling rate. Faster cooling rates promote formation of basketweave microstructure, while lower cooling rates favor formation of larger α colonies [43]. The grain boundary α layer in prior β grain boundaries forms diffusionally and is typically observed in cast and weld materials with lower cooling rate [7].

High energy beam welding processes such as EBW and LBW can have cooling rates between 100 to 1000 °C/s. Microstructures produced by these processes can be entirely martensitic. For arc welding processes such as TIG and PAW, cooling rates between 10 to 150°C/s have been reported, which typically produce a microstructure with a combination of martensitic α’, massive α_m and diffusional α [44].

3.2.3 Post weld heat treatment

Post weld heat treatments are applied on welds to relieve residual stresses, stabilize and homogenize the weld zone microstructure and to improve ductility [44]. Residual stresses are almost fully relieved at 540°C [45]. Microstructural changes occur during post weld heat treatments. In Ti-64, it has been observed that martensitic α’ decomposes to equilibrium α and β. At temperatures below 550°C, coherent Ti_3Al precipitates form which is seen in a rise of hardness of welds post weld heat treated at low temperatures [7], [45]. Martensite decomposition is not completed at temperatures below 600°C. Significant diffusion of aluminum into α phase and vanadium into β phase has been observed at 650°C [45]. A post weld heat treatment temperature of 700 - 800°C is required for complete decomposition of martensite [46]. The microstructure coarsens during post weld heat treatment. At temperatures below 700°C no significant coarsening occurs whereas at temperatures of 800 to 900°C coarsening of the α laths and formation of grain boundary α has been observed [45], [47]–[49]. The hardness of the welds starts to decrease at temperatures above 650°C [45]. The ductility improves with increasing post weld heat treatment temperature but cannot be fully restored in α+β titanium alloys. Fracture toughness is also improved with increasing temperature [44]. Fomin et al. [45] found that the notch sensitivity and high cycle fatigue performance improved with increasing post weld-heat treatment temperature. Two stage heat treatments with recrystallization treatment at approximately 900°C combined with aging at lower temperature provide the transformation of an acicular type microstructure to a coarser colony microstructure with lower strength but improved ductility [45].

3.3 Typical defects in Ti-alloy welds

3.3.1 Cracking and embrittlement

Compared to other alloys such as nickel based superalloys and stainless steels, titanium alloys are not considered susceptible to solidification related cracking because of low concentration of impurities. Titanium alloys have been reported to crack if welded under severe restraint [50], but the Ti-64 alloy has excellent cracking resistance. The absence of precipitate particles, impurities at grain boundaries and low melting temperature phases in most titanium alloys makes them resistant to heat affected zone and liquation cracking [6].

Contamination cracking is a problem for titanium alloys. When titanium is exposed to air, moisture or hydrocarbons at temperatures exceeding 500°C, the material will absorb oxygen, nitrogen, carbon and hydrogen. These interstitial elements inhibit plastic deformation and increase strength but cause a decrease in ductility. Iron or tungsten particles are also reported to cause embrittlement. If the contamination level exceeds a certain amount, residual stresses generated by welding can cause cracking. At increased oxygen contents, weld bead discoloration can occur as well as an increase in the surface hardness of the weld [6]. Contamination cracking can be avoided by protecting the heated weld region from interstitial elements. High purity inert shielding gas needs to be used to shield the weld pool, hot weld bead and the backside of the joint. Thorough cleaning and degreasing of joint surfaces is required [6].

3.3.2 Porosity

Porosity is a concern for high performance components that are subjected to cyclic loading as pores reduce the fatigue resistance of the welds. Several studies indicate a significant decrease in fatigue life of welds containing porosity compared with defect-free welds [51]–[53]. Surface porosity has shown to be especially detrimental. Porosity is a concern particularly in components where the weld profiles are dressed or machined away. In such components the geometrical defects in the weld profile do not affect fatigue life and internal pores can break a surface, and act as stress concentrators [54].

There are many reasons for porosity formation in welding such as shrinkage of the weld material, trapping of shielding gas, chemical reaction in the weld pool, keyhole instabilities, and evaporation [32], [55]–[57]. The pores are often classified based on their shapes; rounded pores are classified as gas pores, irregular pores are classified as shrinkage pores. In titanium alloy welds spherical gas pores are the most prevalent [32].

3.3.2.1 Hydrogen porosity

Hydrogen is recognized as another major cause for porosity in titanium alloy welds. The hydrogen solubility in titanium increases as the temperature decreases. There is a sharp decrease in solubility at the solidification point, which causes the rejection of small hydrogen bubbles in the meltpool as the weld solidifies. Typically, a hydrogen content of 280 ppm is required for hydrogen bubbles to be rejected, which is much more than the hydrogen content in modern titanium alloys [58]. There are other potential sources for hydrogen such as:

- preparation of joint surface
- welding consumables
- shielding gas and
- the hygroscopic titanium oxide layer [51].

Workpiece preparation is essential in avoiding hydrogen porosity. Removal of the hydrated oxide layer and other surface contaminants is important in minimizing the hydrogen content in the meltpool. Mechanical cleaning and chemical pickling with a solution of hydrofluoric acid and nitric acid has been shown to be effective [32], [51]. The time between joint preparation and welding should be minimized, because the oxide layer continues to absorb moisture [32], [56]. Other sources of hydrogen may be the shielding gas or the filler material which is why high-purity shielding gases and extra low interstitial filler materials are used [32].

Hydrogen induced porosity has been reported to occur in various processes. In EBW and several arc welding processes, it has been suggested to be the main reason for porosity [51], [55], [56], [59]. In LBW, the main reason for porosity is suggested to be related to the instabilities in the welding process. Process induced pores are typically larger in size than hydrogen porosity [32], [57], [60].

3.3.2.2 Porosity in laser welding

Weld metal porosity is reported to form easily in keyhole laser welding. Several studies have shown that keyhole instability can lead to metal vapor or inert gas getting trapped in the weld metal [60]–[63]. This occurs when the forces keeping the keyhole open are not in balance with the forces that try to close the keyhole. In the following section, possible sources of formation of process induced porosity and methods to control porosity are reviewed.

Pore formation

Keyhole welding is a complex and unstable phenomenon which has been extensively studied both experimentally and theoretically. Formation of pores and their subsequent movement and escape of the pores in the meltpool are affected by variety of factors. The forces acting on the keyhole and the meltpool during laser welding are primarily determined by the properties of the incident laser radiation (wavelength, power density, etc.), the material properties (thickness, chemical composition), the welding speed and the surrounding environment (the gas utilized to shield the welding process) [27].

Analysis of origin of pore gases has been performed by few authors. Huang et al. [64] showed that the majority of the gas inside a pore was hydrogen with some CO_2 in electron beam welded Ti-64. Studies on laser welded aluminum and magnesium alloys have shown that the gas inside the pores has mainly been hydrogen and argon shielding gas [63]. Successful pore gas analysis on laser welded titanium alloys has not been published [63]. Most of the published studies suggest that the porosity is caused by shielding gas that gets trapped by keyhole instabilities [60], [65], [66].

The incident laser radiation, in terms of total power and power density, can be perturbed by the metallic vapor exiting the keyhole which provides a mechanism for the fluctuation in laser power and, as a result, the keyhole instabilities. Klein et al. [67] showed computationally that fluctuations of 1% in the incident laser power can cause fluctuations in the keyhole causing collapse of the keyhole and formation of defects.

Matsunawa et al. [61] studied the behavior of transient behavior of keyhole during CO_2 laser welding of AA5083 using X-ray transmission imaging method. Despite the constant welding parameters the keyhole exhibited unsteady behavior with fluctuations in penetration depth and the formation of porosity in the weld metal. The observations showed that localized evaporation of metal in the keyhole front wall lead to perturbations in the keyhole rear wall causing bubbles to form.

Panwisawas et al. [60], [68] showed that turbulent meltpool flow can introduce porosity in laser welding of Ti-64. Their model showed that Marangoni flow due to the high thermal gradient during the process is responsible for the recirculation at the melting front which was related to porosity observed in welding experiments. Their model also showed that when the energy density was very high, the flow behavior within the fluid region was predicted to become unstable at the tip of the keyhole. The porosity was mainly dependent upon three parameters: plate thickness, laser power and welding speed.

Pang et al. [65] developed a model for CO_2 laser welding of titanium alloy to predict porosity induced by keyhole instability. The model could predict keyhole depth fluctuations at different welding speeds and found that the fluctuations were closely related to the size and number of pores in the weld beads. The model showed that the temperature and pressure at the tip of the keyhole dropped severely during fluctuation allowing shielding gas to flow into the keyhole and become trapped in a bubble.

Huang et al. [69] simulated laser welding of steel and aluminum alloy. In comparison to steel, the laser welding of aluminum alloy produced a higher depth to width ratio keyhole and more intense melt flow. A deep and narrow keyhole is more unstable and prone to collapse, and more bubbles are formed.

During pulsed laser welding uncontrollable collapse of the keyhole may be a major cause for formation of porosity [62], [66], [70]. Zhou et al. [70] observed that solidification rate, back filling speed of liquid metal and aspect ratio of the keyhole had major influence on the formation of porosity. On wider welds, porosity could be suppressed through laser pulse shape control to delay the solidification process. Narrow welds were most susceptible to porosity. Blackburn et al. [63] showed that pulse frequency and pulse shape had a significant influence on porosity. An oscillating wave was created in the weld pool when low porosity welding conditions were used, which was thought to act in manipulating the ejection angle of the vapor plume and aiding the escape of the gas bubbles in the weld pool.

Bubbles may escape from the meltpool via the keyhole wall or the meltpool surface. Huang et al. [64] showed that pores that nucleate at the leading edge of the melpool during electron beam welding may escape through the keyhole wall because the liquid film at the side of the keyhole is very narrow. The escape of the bubbles was hindered if the liquid film was thicker. Panwisawas et al. [60] observed that occurrence of porosity was dependent on thickness of the material. On thin sheets, no pores were observed despite the model predicting their formation. They suggested that on thin sheets the distance is smaller for the bubbles to escape and thus more probable. Blackburn [63] calculated that if only buoyancy force is considered, larger pores would typically have time to escape the meltpool before solidification. However, the majority of welds produced at slower speeds had a significantly higher amount of subsurface porosity than those produced at higher speeds which suggests that more gas bubbles are formed at slower welding speeds and once these gas bubbles are present in the meltpool, it is difficult for them to escape.

Several methods to suppress the formation of porosity have been introduced in the literature. Welding parameters have a significant influence on formation of porosity. The effect of process parameters, however, appears to be complex and universal strategies for minimizing weld metal porosity have not been established. Typically partial penetration welds exhibit more porosity than full penetration welds [34], [71] with exception of conduction mode welding which is a more stable process than keyhole welding. It appears that parameters producing keyhole with high depth to width ratio are more prone to porosity [66], [69], [72], [73]. Modelling has shown that high velocity melt flow at the keyhole front can cause a vortex at the keyhole tip causing porosity to form. Welding conditions producing lower melt flow velocities have been beneficial in eliminating porosity [68], [74]. Modulation of laser power has been shown to decrease the porosity in keyhole laser welding [63], [75]. High beam quality fiber and disk lasers have been shown to produce welds with reduced porosity in comparison to Nd:YAG lasers [63]. Decreasing the joint gap has been observed to minimize the amount of porosity [76]. Methods to stabilize the keyhole have also been explored. A gas jet directed into the keyhole has been shown to stabilize the keyhole and produce pore free welds. Dual focus lasers have also been investigated. With controlled focus spot separation, a stable elongated keyhole can be formed promoting low porosity welds [63].

Furthermore porosity can be controlled by controlling the welding atmosphere. Vacuum welding has been effective in the prevention of porosity while the same welding parameters in ambient pressure produced porous welds. Also penetration depth increased [77]. Using helium as protective gas instead of argon has produced good results with CO_2 laser welding [78]. Gas jets between the laser head and the workpiece have also produced welds with improved quality when welding with high beam quality [63]. All these methods minimize the metal vapor, ionized shielding gas, and hot gas column above the work piece therefore reducing attenuation and refraction of the incident laser beam.

3.3.3 Geometrical weld profile defects

Geometrical weld profile defects can occur because of the welding process or due to the joint configuration. For example joint misalignment is not directly related to the welding process but occurs more commonly in keyhole laser or electron beam welding because the narrow beam can more easily miss the joint line. Incorrect clamping, restraint or inadequate machining may lead to other geometrical defects [32], [79]. Geometrical defects related to welding process include humping, undercut, slumping, concavity, lack of penetration, burn through, and spatter. Usually it is possible to find a balance of process parameters, such as weld speed and power, to achieve required weld penetration and minimize weld-profile defects. For example, humping is usually observed at high welding speeds [79]. In laser welding, underfill depth has been reported to decrease with increasing welding speed as less evaporation occurs [80].

Titanium has some favorable properties such as good weldpool fluidity, low thermal conductivity, low density and high surface tension. These characteristics are favorable in minimizing weld geometry defects and allow welding with an unsupported root surface [44].

Geometrical weld defects are particularly harmful in components subjected to dynamic loading. The defects at the surface of the components act as stress concentrators and initiate fatigue cracks. In some cases remelting the weld surface or machining can be used to reshape the weld geometry and remove the geometrical defects [54].

3.4 Mechanical properties of welds

3.4.1 Tensile properties of Ti-64 welds

According to Lütjering [7], the important microstructural parameters for fully lamellar microstructures with respect to mechanical properties are the β grain size, the α colony size, the width of the α plates, and presence of grain boundary α layer. The most critical parameter is the size of α colonies which defines the effective slip length. Decreasing α colony size improves the yield strength, the ductility, the micro crack nucleation, and the micro crack propagation resistance, whereas the macro crack propagation and fracture toughness are improved by large α colony size. Large increase in the yield strength is observed when the colony structure changes to martensitic microstructure and slip length equals the width of individual α plates.

Tensile ductility of fully lamellar microstructures is lower in comparison to the bi-modal microstructures. Microvoids can nucleate in the α-β interfaces and due to the large aspect ratio of α platelets, there is a large amount of these interfaces in fully lamellar microstructures. Reducing prior β size has a positive effect on tensile ductility [7], [81]. If the strength difference between the intragranular microstructure and the grain boundary α layer is large, the cracks can nucleate at the grain boundary α layer causing less ductile intergranular fracture [7].

For welds this means that the fine lamellar microstructure formed in the fusion zone and heat affected zone has higher hardness than the base material. The ultimate tensile strengths of welds have been reported to be

925 MPa to 1060 MPa. Welds have been reported to have both higher and lower strengths than the base material depending on the welding process and the post weld heat treatment [44]. The martensitic microstructures formed in high energy intensity processes have typically higher hardness and strength than welds produced by arc welding processes [47].

The tensile ductility of welds is lower in comparison to the base material. Tensile elongation as low as 6% has been reported for the welds, while 11% (cast) to 16% (wrought) elongation is typical for the base material. TIG welds have the lowest ductility while EBW welds have been reported to have the highest [81]–[84]. Post weld heat treatments improve the ductility of the welds but not to the level of the base material [47], [85]. The ductility of welds can also be improved by reducing the prior β grain size. Using pulsed current in TIG welding resulted in welds with smaller prior β grain size and better ductility. The smaller prior β grain size in welds produced by EBW may explain their better ductility in comparison to TIG welds [41], [44], [81], [82].

Fracture toughness and resistance to fatigue crack growth is typically better in the welds than in the base material due to the fine lamellar microstructure [47], [86]. In defect-free structures fatigue cracks occur in the area of lowest strength which in weldments is located some distance from the base material [87]. In welds, the joint geometry, defects, and residual stresses can reduce the fatigue performance significantly [51].

3.4.2 Fatigue

Engineering components are frequently subjected to repeated loads, and the resulting cyclic stresses can lead to microscopic physical damage to the materials involved. This microscopic damage can accumulate with continued cyclic loading even at stresses well below the material's ultimate strength. The microscopic damage can develop into a crack which can lead to failure of the component. This process of damage and failure due to cyclic loading is called fatigue [88].

The fatigue process is usually divided in three stages, the crack initiation, the crack growth and the final fracture as illustrated in Fig. 3.7.

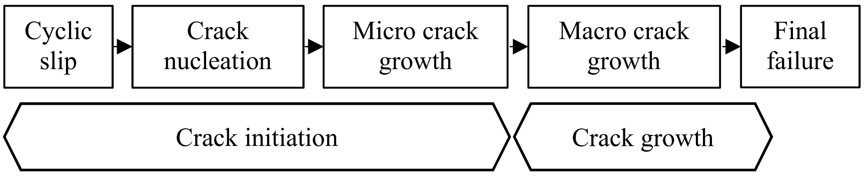

Figure 3.7. Schematic sketch of the different phases for the fatigue failure process. Adapted from [54].

Cracks often nucleate at the surface of the material due to cyclic slip occurring in the planes of maximum shear stress in favorably oriented grains. Micro cracks initiate along these slip lines. The nucleation rate of micro cracks depends to a large extent on the applied loading conditions. In general, with increasing load the number of cycles for fatigue crack initiation decreases. In spite of early crack nucleation, the growth of micro cracks is slow and they remain invisible for a considerable part of the total fatigue life. Once cracks become visible, the remaining fatigue life of a laboratory specimen is usually a small percentage of the total life. The growth of micro cracks is affected by crack growth barriers such as grain boundaries which makes the small crack growth rate irregular or retard the crack growth and turning it into a non-propagating micro crack. Non-propagating cracks can initiate at stresses lower than the fatigue limit [54], [89].

The crack initiation phase is supposed to be completed when micro crack growth is no longer depending on the material surface conditions but the bulk properties of the material are controlling the crack growth rate. The size of the micro crack at the transition to the crack growth depends on microstructural barriers to be overcome and can significantly differ for different materials. Usually, the crack is growing perpendicular to the main principal stress. The final fracture will take place when the crack becomes so large that the remaining part of the cross section is too small to withstand the load and subsequently complete fracture occurs [54].

Cracks nucleate at the free surface because of reduced constraint for slip from adjacent grains, notch effects of surface imperfections and effects of surrounding environment. Cracks can also initiate at grain boundaries or internal inclusions and defects. These defects are normally not considered to be harmful for static strength but could affect the stress distribution on a micro level and thus contribute to crack nucleation [54].

3.4.2.1 Fatigue design methods

There are three major approaches for analysis and design with respect to fatigue: i) stress based approach, ii) strain based approach, and iii) fracture mechanics approach. Since in this project all the fatigue tests have been performed with a stress control approach, the main concepts of this method will be discussed in more detail.

A cyclic loading between maximum stress, S_{max}, and minimum stress, S_{min}, can be characterized by the following values: stress range (ΔS), stress ratio (R), and mean stress S_m.

$$\Delta S = S_{max} - S_{min} \qquad (3.1)$$

$$R = \frac{S_{min}}{S_{max}} \qquad (3.2)$$

$$S_m = (S_{max} + S_{min})/2 \qquad (3.3)$$

Material testing for this approach is done in load-controlled method, testing the material at different stress levels. The results of such a test may be plotted to obtain a stress-life curve, or S-N curve. When the fatigue life, N_f, is plotted against stress range in a log-log plot with sufficient number of data points, a straight line can be fitted to the data. Such a curve is called S-N curve and the corresponding equation will be of the form:

$$\Delta S = A N_f^B \qquad (3.4)$$

, where A and B are fitting constants.

Figure 3.8 shows typical S-N curves. S-N curves vary with material, its processing, stress ratio, chemical and thermal environment, frequency of loading and residual stress. Some materials like low alloy steels and titanium alloys exhibit a fatigue limit or endurance limit, a stress range below which fatigue failure does not occur and life is infinite. For other materials such as aluminum, that do not have a fatigue limit, fatigue strength is defined as stress range at a specific life.

The stress based approach provides a good approximation at low stress levels when the loading causes only elastic strains. This regime is called high cycle fatigue (HCF). If plastic strains are involved the life is shorter and this method fails to model fatigue behavior accurately. The regime of low cycle fatigue (LCF) is better approximated using the strain based approach. The regime where high-cycle fatigue starts varies with material, but is typically from 10^4 cycles or more [88], [90].

The fracture mechanics approach is a technique based on the analysis of fatigue crack growth. It takes into account the pre-existing defects in the material. The pre-existing defects can develop into cracks which can start growing. The fatigue material properties are characterized by the threshold stress intensity range, ΔK_{th}, the fatigue crack growth rate relationship, da/dN vs. ΔK, and the critical stress intensity factor, K_c, which corresponds to the fracture toughness of the material. The cyclic loading is described by stress intensity factor ΔK, which depends on the stresses, geometry parameters and the size and shape of the crack. Two cracks with different conditions, but a constant value of stress intensity factor, will have the same stress field and growth rate [88].

3.4.2.2 Fatigue in welds

Welding is used in a large portion of many engineering structures and it provides numerous structural design options which cannot be realized with other production techniques. However, the fatigue strength of welded structures is normally lower than that of unwelded components. This is also illustrated in Fig. 3.8 which shows schematic stress range - fatigue life curves of i) a smooth plate, ii) a plate with a hole, and iii) a fillet weld [90].

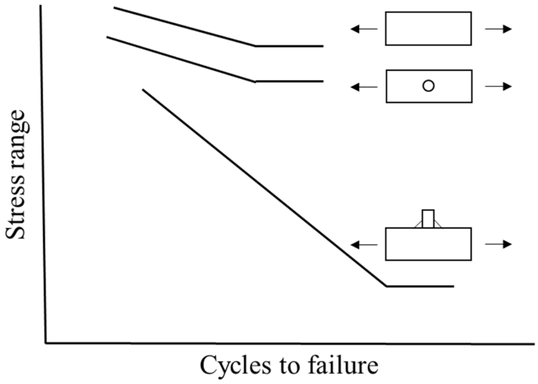

Figure 3.8. Fatigue strength comparison between a smooth plate, a plate with a hole, and a fillet weld. Adapted from [90].

Fatigue strength of welded structures is reduced due to many factors intrinsic to welded joints. The welding process introduces changes to the material that can lead to reduction in fatigue strength. The main factors include stress concentration due to weld geometry, tensile residual stresses and presence of weld defects.

A weld profile causes a change in shape and hence will result in stress concentration. This stress concentration occurs at the toe of the weld that is the junction between the base material and the weld metal which makes it a common site for fatigue cracking in welded joints loaded transverse to the joint [90].

Residual stresses are formed during welding when the weld metal cools down and contracts. This causes tensile residual stresses to form in the weld, compressive residual stresses further away and distortions of the welded structure. The tensile residual stresses can approach the yield strength of the base material which contributes significantly to a reduction of fatigue strength in welded structures [90].

Welding defects such as cracks, slag inclusions, gas pores, lack of penetration at the weld root, and undercut at weld toes may be present in welded joints. Typical defects in titanium alloy welds are discussed in paragraph 3.3 and the effect of defects on fatigue strength is discussed more in paragraph 3.4.2.3.

3.4.2.3 Effect of weld metal porosity on fatigue

As described earlier, welding introduces imperfections to the welding joints which affect the fatigue performance. In situations where the external weld geometry is left intact, fatigue cracking typically initiates at the weld toe. Even if geometry specific stress-raisers, such as weld toes, are removed in order to maximize the fatigue performance of the joints, fatigue strength can still be lowered significantly by the presence of weld metal porosity as shown in Fig. 3.9 [91], [92].

Stress concentrators, such as notches, holes or pores, act to raise the local stress above the stress in the bulk material. The stress concentration factor is defined as the ratio of maximum stress at the stress concentration and the nominal stress which would be present if a stress concentration did not occur ($K_t=\sigma_{max}/\sigma_{\infty}$). Stress concentration factor is based on the assumption of linear elastic material behavior and the severity of stress concentration is affected by the geometry of the notch configuration. Larger stress concentrations are generated when the aspect ratio of the notch decreases or if notches are in close proximity to each other [54], [89].

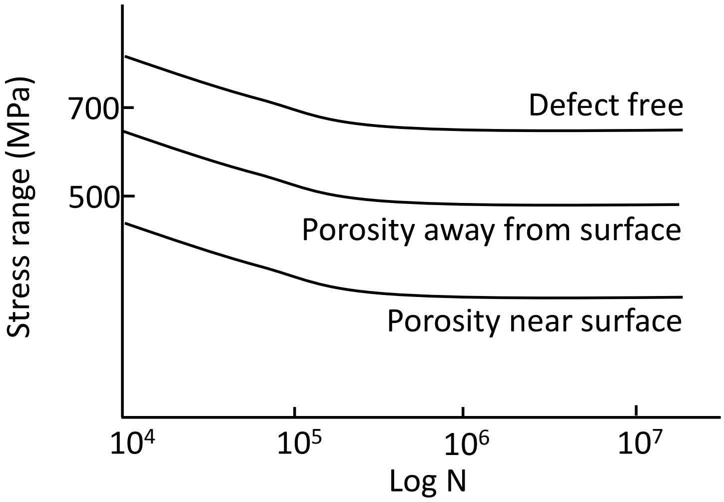

Figure 3.9. Comparison of fatigue data of Ti-64 welds with and without porosity. Adapted from [93].

Finite element modelling of the effect of the proximity of a free surface and other pores has been recently published [53], [94], [95]. Two adjacent pores cause an increased stress concentration if the distance between the pores is less than their diameters [95]. Stress concentration is also increased when a pore is closer than its diameter to a free surface. The stress concentration is at its highest when a pore is just below the surface [95], [96].

In case of fatigue, inclusions and pores can be approximated as small cracks [97]. Therefore, they can be assumed to generate a stress intensity factor which is dependent on the projected area of the defect. The stress intensity factors generated by surface and subsurface defects were formulated by Murakami et al. [97] as follows.

$K_{max} = 0.65\sigma\sqrt{\pi\sqrt{area}}$ (Surface) (3.5)

$K_{max} = 0.5\sigma\sqrt{\pi\sqrt{area}}$ (Subsurface) (3.6)

Equations 3.5 and 3.6 show that defects near the surface will lead to higher stress intensity factor and therefore higher crack growth rate. However, if the size of the crack is small enough, the stress intensity factor can be below the threshold value for crack growth and thus the crack can become a non-propagating crack [97].

4 Experimental techniques

4.1 Materials

A variety of different material batches and alloys were used in this work and their compositions are shown in Table 4.1.

In Papers 1 and 3, Ti-64 sheet material (AMS4911) in annealed condition was used as parent material. For TIG welding Ti-64 welding wire was used.

In Papers 2, 4 and 5, cast Ti-64 with boron additions was used. After casting, the ingots were hot isostatically pressed (HIP) at 900ºC at 100 MPa for 2 hours. The material was delivered by Titanium Castings Ltd, UK.

In Paper 6, 4 batches of sheet material with differing composition were chosen to study the effect of chemical composition of base material on pore formation. All material batches were in accordance with the aerospace material specification AMS 4911N.

Table 4.1. Chemical compositions (in wt-%) of materials used in experimental work.

Paper	Alloy	Type	Al	V	Fe	O	C	N	H	B	Ti
1, 3	Ti64	Sheet	6.12	3.81	0.17	0.12	0.006	0.005	<0.001	0	Bal.
1, 3	Ti64 filler	Wire	5.50-6.75	3.50-4.50	<0.22	<0.18	<0.05	<0.03	<0.015	0	Bal.
2, 4	Ti64-0B	Cast	6.16	4.04	0.20	0.20	0.010	0.002	<0.001	<0.001	Bal.
2, 4	Ti-64-0.06B	Cast	6.24	4.06	0.18	0.19	0.012	0.003	<0.001	0.06	Bal.
2, 4, 5	Ti-64-0.11B	Cast	6.18	4.02	0.19	0.24	0.007	0.004	<0.001	0.11	Bal.
6	Batch1	Sheet	6.08	3.88	0.19	0.14	0.008	0.001	0.0038	0	Bal.
6	Batch2	Sheet	5.92	4.04	0.16	0.17	0.016	0.008	0.0028	0	Bal.
6	Batch3	Sheet	6.23	3.82	0.17	0.14	0.009	0.012	0.0043	0	Bal.
6	Batch4	Sheet	6.13	3.93	0.20	0.16	0.011	0.009	0.0024	0	Bal.

4.2 Welding

The welding experiments were performed by GKN Aerospace Engine Systems in Trollhättan, Sweden.

In Papers 1 and 3, a 4 mm thick Ti-64 sheet material was used as base material to produce welds with TIG, PAW, EBW, and LBW. The EBW, LBW and PAW were produced autogenously and for the TIG weld a filler wire was used. Standard welding parameters were used for the processes.

In Papers 2, 4 and 5, bead-on-plate TIG and LBW welds were produced on 8.5 mm thick sections of cast and HIPed conventional Ti-64 alloy and Ti-64 with 2 different boron concentrations. For TIG welding partial penetration bead-on-plate welds, and for LBW full penetration bead-on-plate welds were obtained.

In Paper 6, bead-on-plate welds on 4 mm thick Ti-64 sheet were deposited using IPG YLR-6000-s 6 kW fiber laser equipped with a 160 mm collimator lens, a 300 mm focal length, and fiber with 0.6 mm diameter.

4.2.1. Design of experiments

A design of experiment (DOE) is a systematic method for planning an experiment that will yield statistically useful results. The simplest way to build an experimental plan is changing one variable (factor) at a time while holding others constant. This approach may fail to capture dependences or interactions among the governing factors and several tests are needed for adequate precision in the estimation of the effect. A more efficient method to study the effect of two or more factors is to vary them simultaneously. Therefore, designed factorial experiments are used when searching for the main contributing factors or the best parameter combination to minimize the variation in a response. DOE describes how an experiment should be performed in order to correlate the controllable and uncontrollable input factors, with the response, while maintaining statistical accuracy and good reproducibility [98], [99].

Depending on the purpose and resources of the experiment, the factors, levels, and ranges of the experiment are set in advance. Typically types of DOEs can be classified as screening designs, characterization designs, and optimization designs. For screening designs, fractional or full factorial designs are typically used. Many factors with few levels are tested to identify most significant factors and the effects of individual factors, the main effects. For characterization designs, the main effects and interactions of small number of factors are studied. Such designs are usually based on full factorial models using two or three levels. Optimization designs are used to study complicated effects and interactions involving one or two factors and may involve several levels to capture nonlinearities [98], [99].

The 2^k factorial designs are a major set of building blocks for many experimental designs. The 2^k refers to designs with k factors where each factor has just two levels and all possible combinations of these levels are considered. In these designs, the levels of factors are referred as high and low; +1 and -1. In most cases, the levels are quantitative, although they do not have to be. 2^k factorial designs can capture linear main effects of factors and interactions between two or more factors. Centre points can be added to 2^k designs to capture quadratic effects and estimating the error [98], [99].

Replication, randomization and blocking are fundamental principles for a well-designed experiment. Selecting experimental units and run sequence randomly helps to restrain systematic errors. Replication is performed to evaluate the experimental error and making statistical tests possible.

Moreover, blocking runs that are similar with respect to a certain factor that cannot be randomized, results in reduction of noise effects. Blocking is especially helpful for experiments that involve people or when all of the experiments cannot be carried out in one single day or with a single batch of material. In a blocked experiment, the block effect can be separated from the effect of other factors [98], [99].

In Paper 6, a blocked 2^k factorial study was designed in order to determine the effect of material variation and welding parameters on weld metal porosity. 4 material batches were chosen on basis of different compositions. The controlled factors in this experiment were welding speed, average power and pulse length. The 4 material batches were treated as blocks and the factorial design was replicated for each material batch.

4.3 Characterization methods

4.3.1 Specimen preparation and optical microscopy

The specimen preparation for microstructural characterization was performed applying conventional metallographic techniques used for titanium alloys. The specimens were cut using cutting wheels developed for non-ferrous metals. Afterwards, the specimens were hot mounted with Struers® PolyFast mounting powder. The subsequent planar grinding and polishing was performed in a Struers® TegraPol-31/TegraForce-5 semiautomatic polishing machine using P240, P320, P800, and P2000 SiC papers. The final polish was carried out using Struers® MD-Chem cloth and OP-S polishing solution. The microstructure was revealed using Kroll's etchant (1 ml HF, 2 ml HNO_3 and 97 ml water).

Light optical microscopy (LOM) is a primary technique for studying microstructure of metallic materials. In this work, a Leica DMRX microscope was used to capture the microstructures of all the investigated materials. Large mosaic images were composed with the Microsoft Image Composite Editor -software.

4.3.2 Scanning electron microscopy

Scanning electron microscopy (SEM) is the most versatile electron microscopy technique and it is one of the most important scientific instruments [100]. SEM provides a wide range of magnifications with high spatial resolution, excellent depth of focus, and allows collection of chemical and crystallographic information. SEM uses a focused electron beam which interacts with matter producing a range of signals that can be detected by different detectors. The smaller wavelength of the electron beam offers significantly higher spatial resolution than visible light in optical microscopy. The electrons are generated in an electron source (tungsten, LaB_6 or field emission gun) and accelerated with voltages between 1 to 30 kV. The electron beam is controlled and focused by means of several electromagnetic lenses and scanning coils. As the electron beam is scanned across the sample surface, electrons interact with the atoms at the sample surface, creating a number of signals. The signals commonly used for imaging are the secondary electrons (SE) and backscattered electrons (BSE), while characteristic X-rays are the most common signal for chemical analysis.

- Secondary electrons are generated by ionization of the atoms in the sample. Secondary electrons are generated in the whole interaction volume but due to their kinetic energy, they can only escape from a depth in the order of 100 nm, providing information of the topography of the sample surface.
- Backscattered electrons result from elastic scattering of the primary electron beam. The interaction volume is larger, approximately 1 µm, which also leads to lower spatial resolution. The backscattered electron yield is affected by the atomic number and the crystallographic orientation which can be used for imaging contrast.
- Characteristic X-rays are emitted when an electron from an outer shell fills a vacancy in an inner shell which was removed by interaction with the primary electrons. The characteristic X-rays have a unique energy depending on the element. The X-rays are emitted from the interaction volume providing spatial resolution of 1-10 µm depending on the energy of the electron beam. Energy-dispersive X-ray spectroscopy (EDS) uses characteristic X-rays for chemical composition analysis [100].

The majority of the SEM work done in this thesis was performed using a FEG-SEM Leo Gemini 1550 which is equipped with an Oxford Nordlys II detector for electron backscatter diffraction and Oxford Inca and Aztec systems for EDS analysis. In this work, SEM was used for fractography using secondary electrons, microstructural characterization using mainly backscattered electrons on unetched samples, and for obtaining crystallographic information by use of electron backscatter diffraction technique.

4.3.3 Electron backscatter diffraction

Electron backscatter diffraction (EBSD) is a characterization technique integrated in SEM systems providing quantitative information of the crystallographic nature of crystalline materials such as grain size, grain shape, grain boundary character, and grain orientation, and allows identification of texture and phases [101]. The schematic representation of the EBSD technique is shown in Fig. 4.1. Kikuchi bands or electron backscatter patterns are obtained in the SEM by focusing a stationary electron beam on a crystalline sample. The sample has to be tilted ~70 degrees out of the horizontal. Upon interaction with the sample, the primary electrons are incoherently scattered and subsequently, the scattered electrons are coherently scattered by the lattice planes, undergoing Bragg diffraction. The generated diffraction pattern is imaged on a fluorescent screen positioned close to the sample and recorded by a highly light sensitive camera. The diffraction cones produce a pattern of Kikuchi bands which can be used to identify the local crystal structure and orientation. Each band in the Kikuchi pattern corresponds to a set of crystallographic planes, the intersections of the bands correspond to zone axes and the pattern center can be used to determine the orientation of the crystal. Hence, with prior information about the expected phases in the material, the EBSD software indexes the acquired EBSD pattern by comparing with the crystallographic information of the expected phases. Performing EBSD analysis over a defined area of the specimen allows acquisition of orientation maps or phase maps [101], [102].

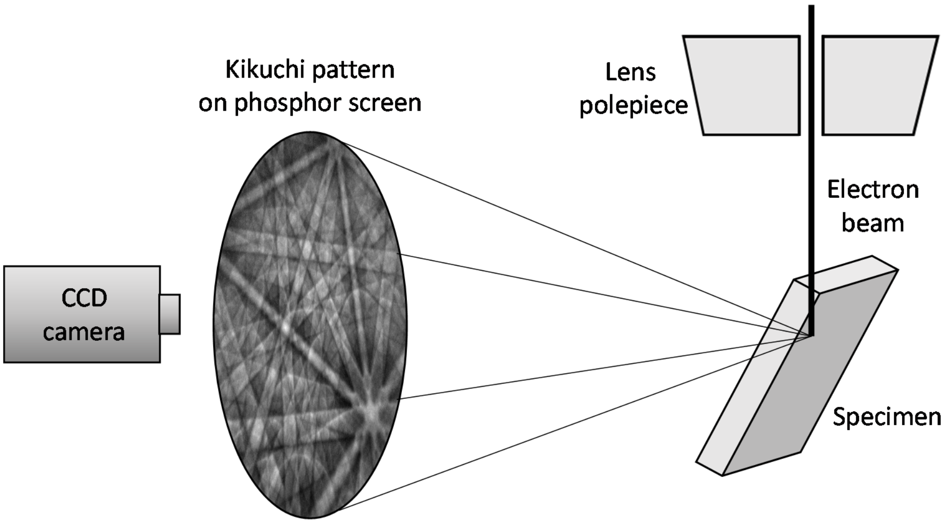

Figure 4.1. Schematic representation of the experimental set up for EBSD. Adapted from [101].

The acquisition and analysis of EBSD patterns is done in different ways according to the purpose. In Papers 4 and 5, EBSD has been mainly used for reconstruction of parent β phase from measured α phase. Scanning electron microscopy (SEM) and EBSD analyses were performed with a Zeiss Leo Gemini 1550 SEM equipped with Nordlys II detector and HKL Channel 5 software. A 4 µm step size was used to acquire overview orientation maps across the fusion zone, the heat affected zone and the base material. EBSD analyses were performed on unetched samples. The process of β phase reconstruction is described in the following section.

4.3.3.1 Beta grain reconstruction

Pure titanium and many titanium alloys undergo a solid state phase transformation from β phase to α phase as they cool down from above β-transus temperature. The solid state β-α transformation disguises the prior β grain structure in a similar manner as austenite to ferrite/bainite/martensite transformation in steels. This is illustrated in Fig. 4.2. As shown earlier, prior-β grain structure has an effect on mechanical properties of welds. Hence, it is import to be able to study the prior-β grain structure. Methods for β grain reconstruction have been developed for example by Germain et al. [103], Cayron et al. [104], Glavicic et al. [105], Davies et al. [106], Simonelli et al. [107], and Yang et al. [108]. The methods have different levels of automation as well as different approaches for α domain and β grain identification and for calculating the orientations of β grains.

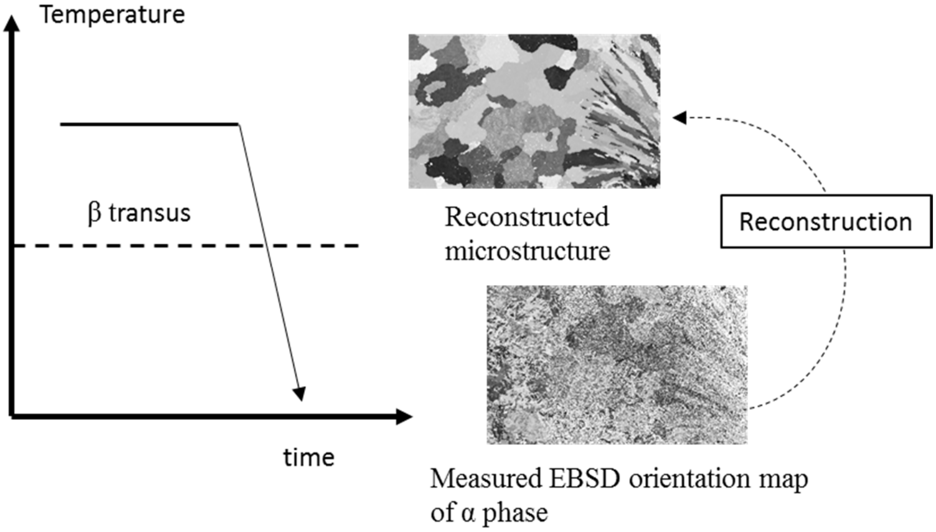

Figure 4.2. Application of the reconstruction technique to evaluate parent β grain structure from measured α phase.

The phase transformation between high temperature β phase (bcc) and low temperature α phase (hcp) follows the Burger's orientation relationship (BOR). According to the BOR the close-packed planes and the nearest-neighbor directions, correspond to each other [5]:

$\{110\}_\beta // \{0001\}_\alpha$ and $<111>_\beta // <11\bar{2}0>_\alpha$ (5.1)

There are 6 {110} planes in β phase, each of which shares two α variants as shown in Table 4.2. Therefore, there are 12 possible α variants that can originate from a single β grain. The possible variants are listed in Table 4.2. By comparing all 12 variants, 12 misorientation angles can be computed. Due to crystal symmetry, misorientation angles between some of the variants are identical. It turns out, that there are only five independent misorientation angles between the α variants originating from a single β grain [4], [109].

Table 4.2. Twelve possible variants generated by the β to α transformation through the Burgers orientation relationship [109].

Variant	Plane parallel	Direction parallel	Rotation angle from V1
V1	$(1\bar{1}0)_\beta \,//\, (0001)_\alpha$	$[111]_\beta \,//\, [11\bar{2}0]_\alpha$	-
V2	$(10\bar{1})_\beta \,//\, (0001)_\alpha$	$[111]_\beta \,//\, [11\bar{2}0]_\alpha$	60°
V3	$(01\bar{1})_\beta \,//\, (0001)_\alpha$	$[111]_\beta \,//\, [11\bar{2}0]_\alpha$	60°
V4	$(110)_\beta \,//\, (0001)_\alpha$	$[\bar{1}11]_\beta \,//\, [11\bar{2}0]_\alpha$	90°
V5	$(101)_\beta \,//\, (0001)_\alpha$	$[\bar{1}11]_\beta \,//\, [11\bar{2}0]_\alpha$	63.26°
V6	$(01\bar{1})_\beta \,//\, (0001)_\alpha$	$[\bar{1}11]_\beta \,//\, [11\bar{2}0]_\alpha$	60.83°
V7	$(110)_\beta \,//\, (0001)_\alpha$	$[1\bar{1}1]_\beta \,//\, [11\bar{2}0]_\alpha$	90°
V8	$(10\bar{1})_\beta \,//\, (0001)_\alpha$	$[1\bar{1}1]_\beta \,//\, [11\bar{2}0]_\alpha$	60.83°
V9	$(011)_\beta \,//\, (0001)_\alpha$	$[1\bar{1}1]_\beta \,//\, [11\bar{2}0]_\alpha$	63.26°
V10	$(1\bar{1}0)_\beta \,//\, (0001)_\alpha$	$[11\bar{1}]_\beta \,//\, [11\bar{2}0]_\alpha$	10.53°
V11	$(101)_\beta \,//\, (0001)_\alpha$	$[11\bar{1}]_\beta \,//\, [11\bar{2}0]_\alpha$	60.83°
V12	$(011)_\beta \,//\, (0001)_\alpha$	$[11\bar{1}]_\beta \,//\, [11\bar{2}0]_\alpha$	60.83°

All the β grain reconstruction methods are based on the Burgers orientation relationship. EBSD technique allows the measurement of the orientations of the transformed α phase. The method developed by Germain et al. [103] is described here in detail. The Merengue 2-software is based on the method described. The method is an iterative process and follows the following steps.

1. Correction of the as measured α phase EBSD map
2. Identification of α domains
3. Identification of α variants originating from the same parent β grain
4. Determination the orientation of the β grain
5. Management of ambiguity

The as-measured EBSD orientation maps for α phase can contain a fraction of non-indexed and/or mis-indexed points. Therefore, in most cases, the as measured α-orientation maps need to be corrected before applying the reconstruction method. The correction can be done using a commercial EBSD software that allows to identify wild spikes and consider them as non-indexed pixels. In a second step, the non-indexed pixels can be reduced by assigning them the orientation of their neighboring pixels.

The α domains or colonies are then identified using an ALGRID grain identification algorithm which improves identification of weakly misoriented α domains. Reliable identification of α domains is a prerequisite for reliable β grain reconstruction.

The α variants originating from the same parent β grain are identified by comparing the misorientation angles between variants. The α variants related to the same parent follow the misorientation angles shown in Table 4.2. The α variants originating from the same β grain follow the misorientation angles with their direct neighbors but also with all the other variants inherited from the same parent. Checking all misorientation combinations between variants makes it possible to recognize those stemming from the same parent.

Determination of the orientation of β grains is performed by calculating the possible parent grain orientations for each α variant originating from the parent grain. For a single α variant there exists six potential parent β grain orientations. The potential parent grain orientations from all the considered α variants are weighted by their surface fraction. Potential parent grain orientations are compared and the orientation with maximum surface fraction is assigned. Because of the statistical nature of the approach, the method is useful in data sets where small amounts of wrongly indexed pixels are found.

In Papers 4 and 5, the effect of boron on prior-β grain structure was studied with EBSD analysis combined with prior-β grain reconstruction performed by the *Merengue 2* software.

Method based on removal of intervariant boundaries

A method based on removing the grain boundaries between the α variants was also explored. According to the Burgers orientation relationship, each prior-β grain can transform into up to 12 different orientation variants of α. As shown in Table 4.2, these variants have specific misorientation angles and axes between them. HKL Channel 5 software allows to disregard grain boundaries with specified misorientations. Figure 4.3 shows the result of a reconstruction with this method.

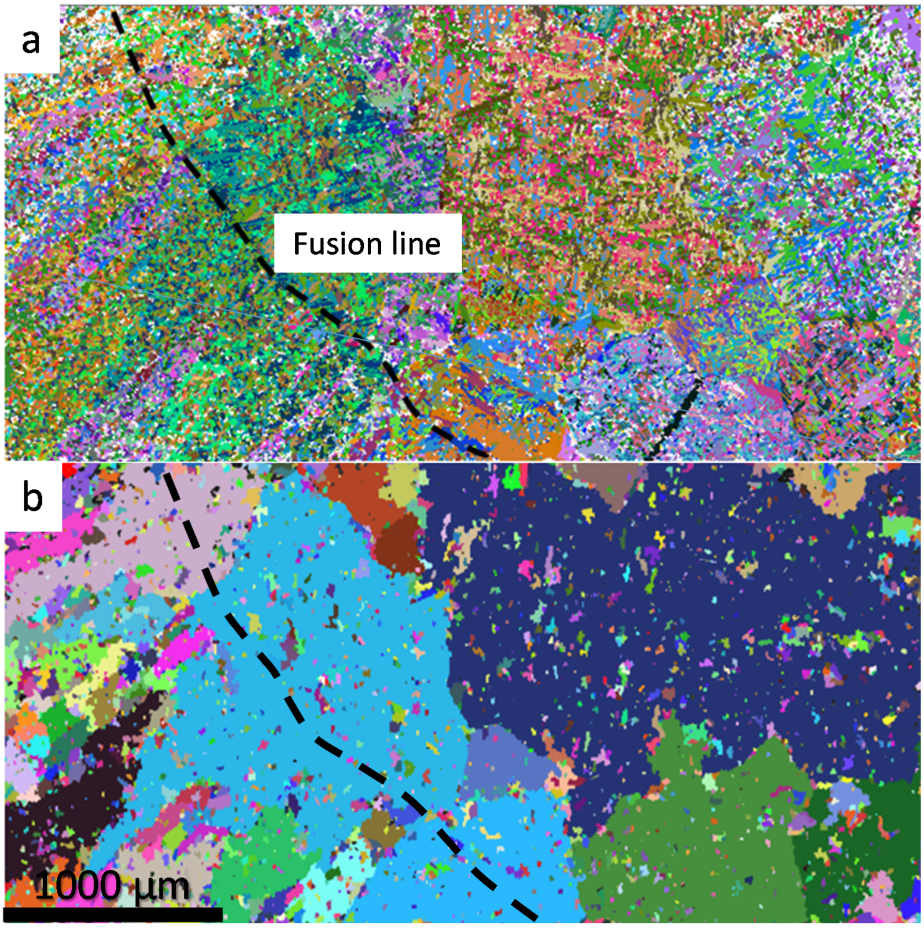

Figure 4.3. a) Orientation map of α phase and b) reconstructed β phase map using HKL Channel 5 software. Both maps are shown in Euler angle coloring.

The principle of this method of prior-β reconstruction is simple and efficient but, in practice, it proved to be difficult and ultimately unsuccessful. As shown in Fig. 4.3, some of the prior-β grain boundaries are captured. However, it appears that several prior-β grain boundaries have been incorrectly removed. Numerous tiny grains also show that all the grain boundaries between the α variants originating from the same parent grain were not identified.

This method has some drawbacks. First, it is possible that α variants originating from different β grains may, in some cases, have misorientation angles that match the ones shown in Table 4.2. This leads to removal of this intervariant boundary and ultimately the two β grains are combined. Another drawback is the fact, that the β to α transformation does not follow the Burgers orientation relationship strictly but there are small deviations in the orientations of the α variants [110]. Therefore, a more advanced method was required for successful β grain reconstruction.

4.3.4 Quantitative image analysis

The quantification of microstructure features in α/β titanium alloys is quite difficult because the microstructure is complex. It involves features spanning a wide range of size scales. Stereological analysis procedures have been studied for titanium alloy Ti-64 [111], [112]. They suggested measuring methods for most of the microstructure features in titanium alloy Ti-64 using Adobe Photoshop software with FoveaPro add-in, a set of functions for computer-based image processing and measurement in images. However, in welded Ti-64, the microstructural features are very fine and the contrast in the images was not sufficient for automated image processing. Thus, in the present work, quantitative image analysis was performed manually using ImageJ software. Images for quantitative image analysis were acquired using optical microscopy or SEM using backscattered electrons on unetched samples.

Phase fraction

The volume fraction of phases was evaluated by measuring the area fractions of different phases from SEM-BSE micrographs. In the original grey scale SEM-BSE image (Fig. 4.4), α phase is seen in dark and the β phase in bright color. The difference in composition generates the contrast between the phases. To confirm the phase contrast produced by backscattered electrons, EDS and EBSD were used. The phases were separated using thresholding to generate a binary image. The method was used to evaluate phase fraction of TiB phase in Paper 4 and the base material β phase fraction in Paper 6.

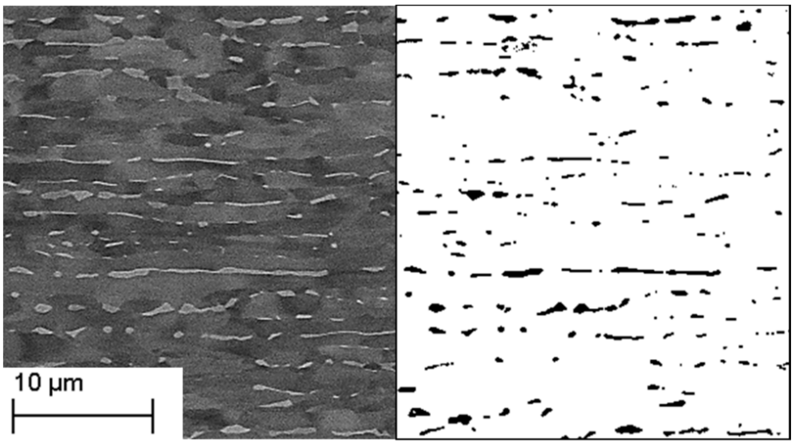

Figure 4.4. Example of α and β phase fraction evaluation in Ti-6Al-4V using thresholding technique.

Size of prior-beta grains and alpha colonies

The prior-β grain sizes and α colony sizes were estimated by a size factor using a mean intercept length method. The colony size factor is the average length of a randomly oriented line that intersects the colony. The colony size factor has a dimension of length that represents the colony size; it is called "size factor" because it does not give any information regarding the shape of the colonies. A set of random lines is drawn in a micrograph; all the intersections of those lines with the colony boundaries are marked (Fig. 4.5). A numerical value for the colony size factor is then obtained by dividing the total line-length by the total number of marked intercepts [112]. The size of prior-β grains was evaluated in a similar manner.

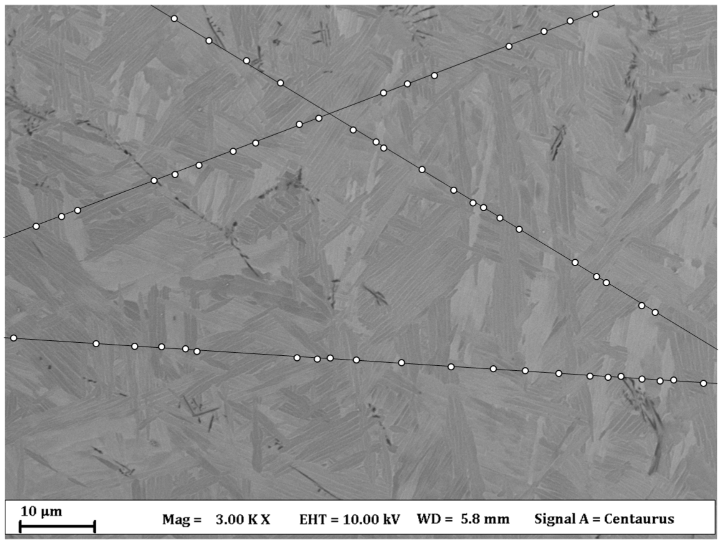

Figure 4.5. SEM-BSE micrograph used for measuring the colony size factor. The black lines are randomly placed and the intercepts of the lines with the colony boundaries marked with white circles.

Thickness and length of alpha laths

To measure the thickness of α laths, a set of random lines is drawn on the image. The intercept length, λ, is calculated by dividing the total line length with the number of intercepts where the line crosses the β phase. By inverting the lengths and calculating the mean value, $(1/\lambda)_{mean}$, the mean thickness of the laths was calculated from the following relation:

$$thickness = \frac{1}{1.5\left(1/\lambda\right)_{mean}} \qquad (4.1)$$

The factor 1.5 comes from the stereological relationship by which the thickness of infinite α laths can be estimated by the line segments which are the intersections of the lines with those α laths [112].

In paper 4, the length of α laths was evaluated by measuring the 15 longest α laths in each SEM micrograph. A minimum of 15 micrographs was used to evaluate the α lath length in HAZ and FZ of welds with different boron contents.

4.3.5 Fractography

By characterizing the topography of the fracture surface, information about the cause of crack initiation and fracture mechanisms can be revealed. Fatigue failure can be divided into different stages, i.e. crack initiation, crack propagation and final fracture. Figure 4.6 shows a crack initiation at a pore, a relatively flat crack propagation area around the initiation and the final fracture surface.

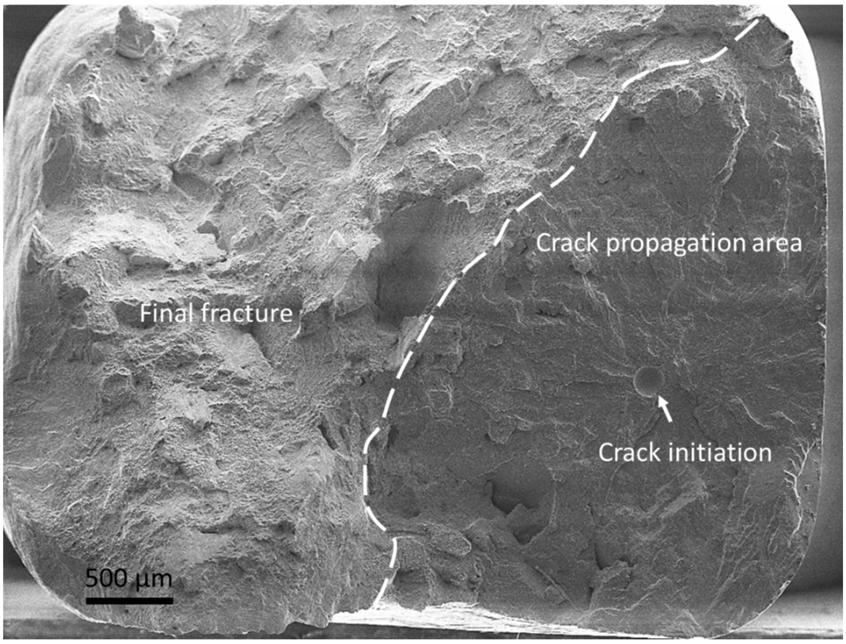

Figure 4.6. Fracture surface of a fatigue specimen.

In Papers 1 and 3, fractography was carried out on the fracture surfaces of fatigue-tested samples. The type, size and location of the crack initiation sites were recorded. In addition, tensile tested samples were investigated in Paper 3. Fractographic evaluation was carried out in a LEO Gemini 1550 FEG scanning electron microscope.

4.4 Mechanical testing

The tensile testing and the low cycle fatigue testing were carried out by an ISO 17025 certified commercial mechanical testing laboratory. Below, the details from the performed mechanical testing are provided.

4.4.1 Tensile testing

The strain controlled tensile testing at room temperature was performed according to ASTM E8. The testing carried out at 250°C was performed according to ASTM E21. The tensile testing was performed in transverse direction to the weld.

4.4.2 Fatigue testing

The load controlled fatigue testing (Paper 1 and 3) at room temperature and at 250°C was performed according to ASTM E466. In Paper 3, a set of polished and unpolished LBW specimens was also tested at 200°C.

Figure 4.7 shows the removal of the external weld geometry from tensile test samples and LCF samples. The fatigue specimens were polished in order to study the effect of microstructure and internal defects. In addition, a set of unpolished laser beam welded samples were tested to determine the influence from the external weld geometry.

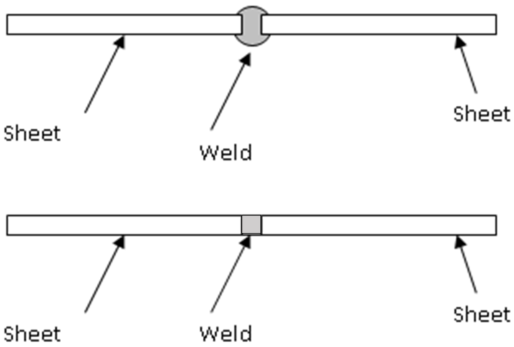

Figure 4.7. Schematic sketch of the LCF specimen geometry. Removal of the external weld geometry.

Specimens for fatigue testing were prepared in longitudinal and transverse direction to the weld as shown in Fig 4.8. Equal amount of samples were tested in both directions.

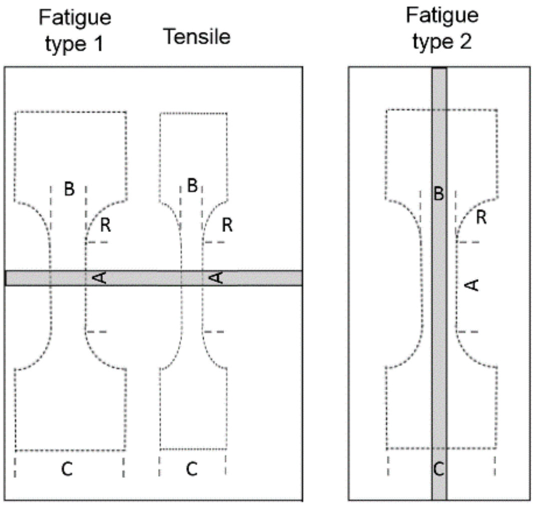

Sample dimensions (mm)

	TIG, EBW, LBW		PAW	
	Fatigue	Tensile	Fatigue	Tensile
A	25	25	20	20
B	6	4	4	3
C	23	18	19	13
R	10	7.5	10	5

Figure 4.8. Schematic drawing and table with dimensions of the fatigue test specimens.

4.4.3 Hardness measurement

Vickers hardness measurements were performed with a Shimadzu HMV-2000 hardness tester using a load of 300 g or 500 g for 12 seconds and a Wolpert 2RC hardness tester using a load of 5 kg for 12 seconds.

4.5 X-ray techniques

4.5.1 X-ray radiography

The principle of X-ray radiography is illustrated in Fig 4.9. A 3-dimensional object is projected onto a 2-dimensional plane, i.e. the detector. The detector can be a film or a CCD detector. X-rays are generated in an X-ray tube when a beam of electrons is accelerated on to a target by a high voltage and stopped suddenly on striking the target. X-rays interact with the object by scattering and absorption. As the X-ray beam passes through material, photons get absorbed or scattered so the intensity of the X-ray beam is reduced; this is known as attenuation. The advantage of conventional X-ray radiography is the high efficiency for porosity detection in large components. As disadvantages can be named the overlap of different defects, the difficulty to detect planar defects, and the relatively low spatial resolution [113].

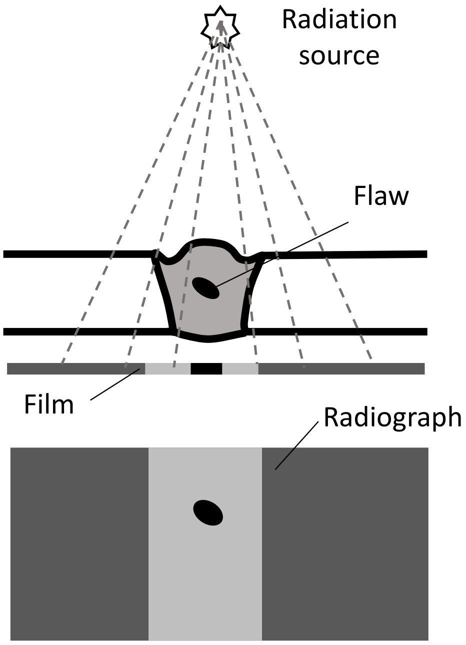

Figure 4.9. Illustration of a basic radiographic set-up. Adapted from [113].

Radiographic sensitivity is a measure of the quality of an image in terms of the smallest detail or discontinuity that may be detected. Radiographic sensitivity is dependent on the object, the scattering, the detector, and geometric factors. Geometric unsharpness refers to the loss of definition that is the result of geometric factors of the radiographic equipment and setup. It occurs because the radiation does not originate from a single point but rather over an area. As shown in Fig. 4.10, there are three factors controlling unsharpness: size of the X-ray source, source to object distance, and object to detector distance. The source size is obtained by referencing the manufacturer's specifications for a given X-ray source. Industrial X-ray tubes often have focal spot sizes of 1.5 mm but micro focus systems have spot sizes in the 30 μm range. As the source size decreases, the geometric unsharpness, or the size of penumbra (U_g) also decreases. The resolution of conventional X-ray radiography can approach around 2% of the thickness of the specimens. Image quality indicators mimicking different defect types are used to estimate the capability of a radiographic technique [113].

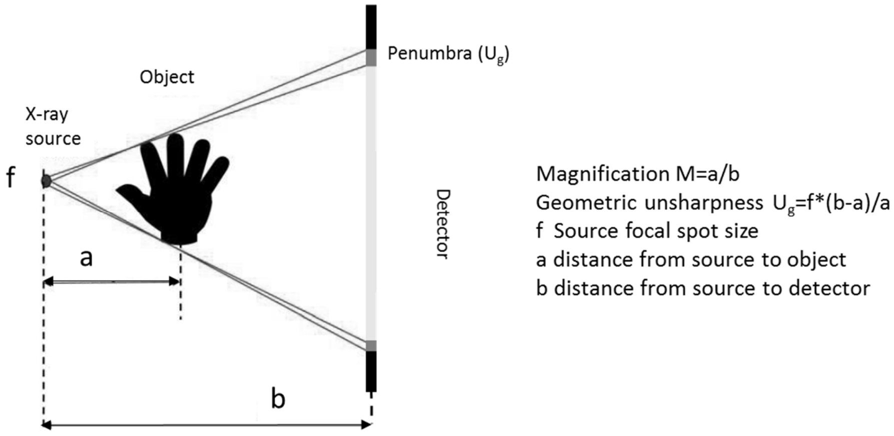

Figure 4.10. Schematic visualization of image magnification and geometric unsharpness. Adapted from [114].

In this work conventional X-ray film radiography was used to characterize porosity in Paper 6. Radiographic examination of all bead-on-plate welds was performed using Yxlon 160 kV X-ray tube with X-ray film.

4.5.2 X-ray tomography

A schematic illustration of steps involved in X-ray computed tomography is shown in Fig. 4.11. In a laboratory X-ray imaging equipment, X-rays are generated by an X-ray source. The X-ray beam is directed towards a detector with the sample being placed between the source and the detector. As the X-ray beam passes through the sample, some of the photons are attenuated. The attenuated beam intensity is measured by the detector as the sample is rotated and radiographs are recorded for each rotation step. The rotation steps used are typically between 0.1° and 1°. The series of projected images is then used to reconstruct a 3D matrix where each element is referred as voxel. The value of a voxel corresponds to the X-ray attenuation at that point in the sample [113]–[115].

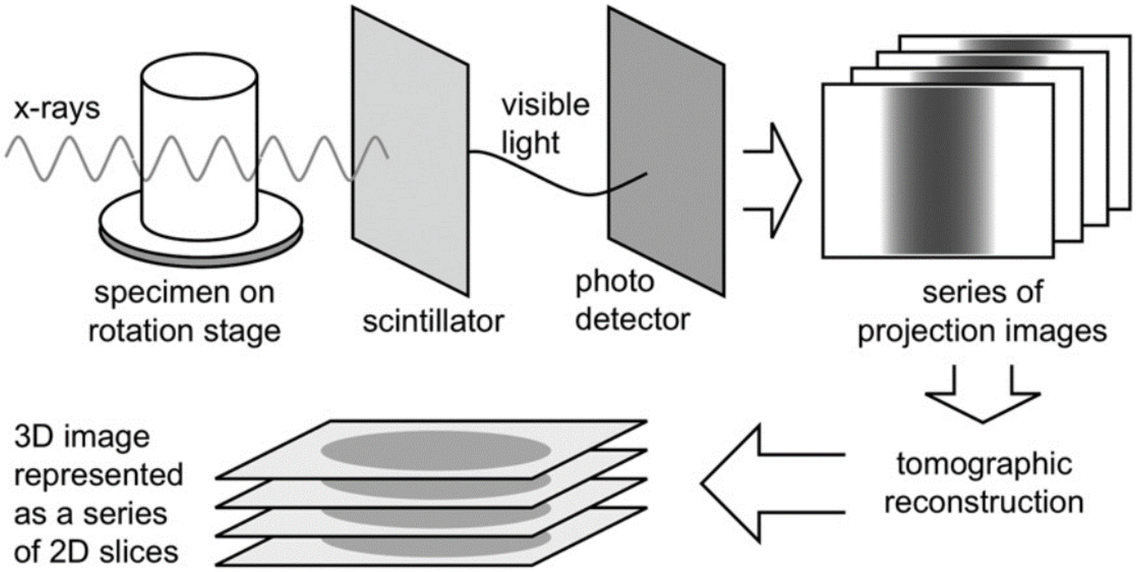

Figure 4.11. Schematic illustration of X-ray computed tomography process. Reprinted from [115], with permission from Elsevier.

The most common method to reconstruct a 3D volume from the series of 2D projections is called filtered back-projection technique. Back-projection reconstructs an image by taking each view and smearing it along the path it was originally acquired. The final back-projected image is then taken as the sum of all the back-projected views. The resulting image is a blurry version of the correct image. In the filtered back-projection technique, blurring is reduced by applying a filter to each recorded view before back-projecting them. The back-projection of the filtered radiographs results in a much sharper image [116].

Magnification in X-ray tomography is typically achieved through geometric enlargement as illustrated in Fig 4.10. The image quality in X-ray tomography is dependent on the size of the X-ray source, geometrical factors, and the detector. The resolution of X-ray tomography systems has been improved by using micro- and nanofocus X-ray sources. With these sources X-ray micro-tomography can reach resolution down to 1 µm. The resolution of micro-tomography equipment quickly decreases as the sample size increases. This is due to geometrical factors and the fact that higher intensity X-rays are needed for sufficient penetration. In general, the X-ray source size increases with the beam current [113], [115]. X-ray microscopy (XRM), developed by Carl Zeiss Microscopy, uses optical magnification in addition to the geometric magnification to achieve higher resolution. Sample images are initially enlarged through geometric magnification as they are in conventional micro-tomography. The projected image impinges on a scintillator, which converts X-rays to visible light, which then is subsequently magnified by an optical objective before reaching the detector. Spatial resolution down to 50 nm can be achieved by XRM equipment [117].

In Paper 3, XRM investigations were performed on selected LCF specimens using Zeiss Xradia 520 Versa equipment located at the Zeiss Microscopy Customer Center in Oberkochen, Germany. The scan volume was 3 mm x 5 mm x 8 mm with 4 µm voxel size, and 3 mm x 5 mm x 1 mm with 1 µm voxel size.

In Paper 4, X-ray micro-tomography was used to study porosity in boron alloyed laser welds. The porosity in the welds was examined with a Nikon XTEK XTH 225 kV X-ray micro-tomography system. A 27 mm long section of each laser weld was scanned and the dimensions of the examined volumes were approximately 8.5 mm x 8.5 mm x 27 mm. The reconstruction was done using a voxel size of 5 µm. The X-ray tube settings (180 kV, 130 µA) produced a focal spot size of approximately 20-25 µm. The geometric enlargement was 23.5x, and the detector pixel size 127 µm. With these conditions the geometric unsharpness was 0.5 mm and the smallest detectable defect size was in the range of 20 µm.

4.6 Chemical analysis

Chemical compositions of base materials and welds were analyzed by SEM-EDS, electron microprobe-analyzer (EPMA), X-ray fluorescence spectroscopy, inert gas fusion, and combustion analysis.

4.6.1 EPMA

Electron probe microanalyzer (EPMA) is a type of electron microscope used to provide chemical information. The operating principle of the electron probe micro analyzer (EPMA) is based on directing a focused electron beam on the sample surface and collecting the characteristic X-ray photons emitted by the various elements in the sample. The characteristic X-rays are recorded using wavelength-dispersive spectroscopy (WDS). The WDS detector provides better spectral resolution and shorter detector dead time than SEM-EDS systems. This provides better sensitivity for analyzing light elements such as O, N and C. EPMA is considered as fully qualitative and quantitative method for elemental analysis of submicron-sized volumes at the sample surface with sensitivity in parts per million (ppm) [100].

EPMA was used in Paper 3. A JEOL JXA-8500F electron probe micro analyzer was used to analyze the oxygen and aluminum content of TIG and EBW welds in comparison to the base material. Measurements were performed at the Norwegian University of Science and Technology (NTNU) in Trondheim. Qualitative line scans across the welds were performed using an acceleration voltage of 10 kV, a beam current of 30 nA, a step size of 100 µm, and a 5 µm defocused beam. Quantitative analysis was not performed due to lack of standard material.

4.6.2 Chemical analysis by Degerfors Laboratorium

The amount of hydrogen, oxygen and nitrogen were determined using inert gas fusion method which was carried out according to ASTM E1447 and ASTM 1409 standards. In inert gas fusion method, the test sample is fused in a graphite crucible under a flowing inert gas stream at a temperature sufficient to release O, N and H. Oxygen combines with carbon to form carbon monoxide (CO) while nitrogen and hydrogen are released as N_2 and H_2, respectively. The released gases are swept by the inert gas stream and analyzed by an infrared or thermal conductivity detector. Uncertainty of measurement is 0.001% for H and 0.01% for O and N [118], [119].

The amount of carbon is determined by combustion analysis which was carried out according to ASTM E1941 standard. In combustion analysis, a metal specimen is combusted in an oxygen atmosphere in an induction furnace. The carbon in the specimen is oxidized to carbon dioxide or carbon monoxide, or both, and is eventually carried to the detector. Uncertainty of measurement is 0.002% [120].

The amount of Ti, Fe, Al, and V were determined by X-ray fluorescence spectroscopy which was carried out according to ASTM E549 standard. In X-ray fluorescence spectroscopy, a specimen is irradiated by high-energy X-ray photons. Secondary X-rays are produced and emitted from the sample. This radiation is measured by a detector, which measures the count rates at specified wavelengths. Mass fractions of the elements are determined by relating the measured radiation from samples to calibration curves prepared using reference materials of known compositions. Uncertainty of measurement is 0.004% [121].

In Paper 6, the aforementioned methods were used to analyze the chemical compositions of the base material and the weld metal. The analyses were carried out by Degerfors Laboratorium AB.

5 Summary experimental results and discussion

This thesis is the result of the work carried out over five years, which led to the six appended papers. Each paper has its own research focus which contributes to the research objectives outlined in section 1.1.

- In Paper 1, the effect of defects and microstructure on fatigue strength of Ti-64 welds produced by PAW and TIG was studied. The welds were fatigue tested and the weld microstructure, fracture surfaces, crack initiation sites and internal defects such as porosity were studied.
- In Paper 2, the microstructures and microhardness of TIG and laser welds performed on cast Ti-64 with boron contents of 0 wt-%, 0.06 wt-% and 0.11 wt-% were characterized. An addition boron to refined the solidification microstructure and α-colony size dramatically in the Ti-64 welds.
- In Paper 3, the effect of microstructure and especially of defects on mechanical properties of Ti-64 welds produced by TIG, PAW, EBW and EBW were studied. The welds produced with different processes have different microstructures and different populations of defects in terms of their size and distribution. The effect of these aspects on mechanical properties under different testing conditions were investigated.
- In Paper 4, the effect of small additions of boron in cast Ti-64 on the microstructure and porosity of laser welds was investigated. The boron addition was found to refine the prior-β grain structure in the weld zones significantly. The TiB particles that exist in the as cast alloys restricted grain growth in the HAZ and decreased in size in the FZ. Boron addition affected the spatial distribution but not the amount and size distribution of porosity.
- In Paper 5, a method of prior-β reconstruction based on Burgers orientation relationship was applied to study the prior-β grain structure in the different weld zones. The prior-β reconstruction could be performed successfully and the reliability of the reconstruction was evaluated. The fine microstructure in the weld zones together with low magnification resulted in a relatively low indexing rate in the FZ and HAZ which did not affect the quality and reliability of the prior-β grain reconstruction.
- In Paper 6, the effect of material variation on porosity in laser welding of titanium alloy welds was investigated. Laser welding was performed on 4 selected material batches with differing composition. The material batches were characterized in terms of microstructure and chemical composition and the laser welds in terms of porosity, weld geometry, microstructure and chemical composition. 2 out of 4 material batches were found to be significantly more sensitive to formation of porosity. Formation of porosity could be suppressed with choice of welding parameters in all batches.

5.1 Microstructure of welds produced by TIG, PAW, LBW and EBW

Tungsten inert gas welding (TIG), plasma arc welding (PAW), laser beam welding (LBW) and electron beam welding (EBW) are all processes capable of creating high quality fusion welded joints in titanium alloys. Due to the different characteristics of the welding processes, the welds have different microstructures and different populations of defects in terms of their size and distribution. As shown in Fig 5.1, the welding process had significant effect on microstructure of the welds. The TIG weld was widest and contained the largest prior-β grains. The fusion zone (FZ) and prior-β grain size was smaller in PAW than in TIG welds. Welds produced by EBW and LBW were considerably narrower. LBW had the smallest weld zone and smallest prior-β grain size. Also, the prior-β grains in LBW were more equiaxed as compared to the other welds where prior-β grains are elongated.

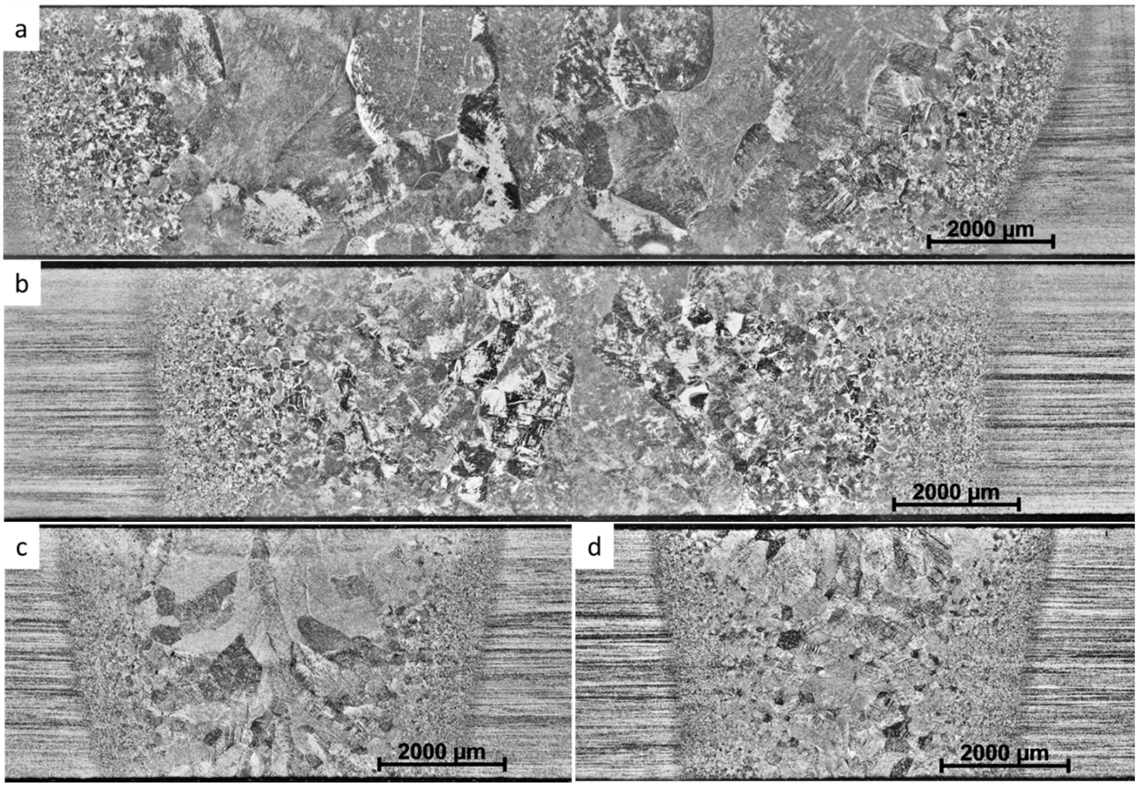

Figure 5.1. Optical micrographs showing the weld cross sections for a) TIG, b) PAW, c) EBW, and d) LBW welds, in 4mm thick Ti-64 sheet material.

Welded α+β titanium microstructures are complex. In all type of welds, the microstructure consisted of fine α plates separated by thin layers of β phase. The thickness of the individual α plates in EBW and LBW samples was on average below 1 µm and in TIG and PAW on average 1.2-1.3 µm. The microstructure of EBW and LBW welds showed features of acicular α' which is a result of martensitic transformation during fast cooling when welding. Upon post weld-heat treatment at 704°C, existing martensite has decomposed into α and β phases, but α laths have retained acicular morphology [46]. The resulting microstructure in EBW and LBW samples is a fine basketweave type of structure. TIG and PAW processes have larger heat input and slower cooling rates which results in a mixture of martensitic and diffusionally transformed products. TIG welds have more of a colony type of microstructure whereas PAW mainly contains the basketweave type of microstructure.

The size and amount of porosity in the welds was estimated by investigating fracture surfaces and performing an XRM study on selected samples. Comparing the pore size distribution in different welds, it can be seen that the pores produced in EBW are the smallest followed by PAW. TIG and LBW produced welds with more porosity and larger in size. In LBW continuous porosity with small pore size was found along the centerline in the weld, with occasional large pores at the root side of the weld. In TIG, the porosity seemed to be scattered.

It should be noted that the microstructural features presented here were achieved using company standard welding parameters. Microstructure and formation of defects can be controlled with welding parameters. However, the results presented here are in line with literature. Arc welding processes have significantly higher heat input producing wider welds with coarse microstructure. Laser and TIG welding are more susceptible to formation of porosity than PAW and EB welding.

5.2 Mechanical properties of welds produced by TIG, PAW, LBW, and EBW

The microhardness of the welds was found to be higher as compared to the base material. Despite the higher hardness of the welds, all the welds fractured in the fusion zone during tensile testing and fractures were found to be a combination of transgranular and intergranular fracture. The tensile ductility was lowered, and TIG and PAW showed the lowest ductility. The tensile ductility depends on the strength difference between the prior-β grain boundary layer and the intragranular microstructure. The high strength of the fine α microstructure inside the grains concentrates the strain in the grain boundaries with lower strength. In addition, the prior-β grain size is related to tensile ductility [7]. Therefore, the larger prior-β grain size found in the TIG welds could explain the lower ductility. TIG welds had the largest prior-β grain size, followed by PAW that also had lowered ductility. LBW and EBW had the smallest prior-β grains and also showed the highest ductility. Titanium alloys are very reactive at elevated temperatures and pick up of interstitial elements such as O, N and C during welding has been suggested as a reason for lowered ductility [122]. However in this case, EPMA measurements did not reveal elevated oxygen levels in TIG and EBW.

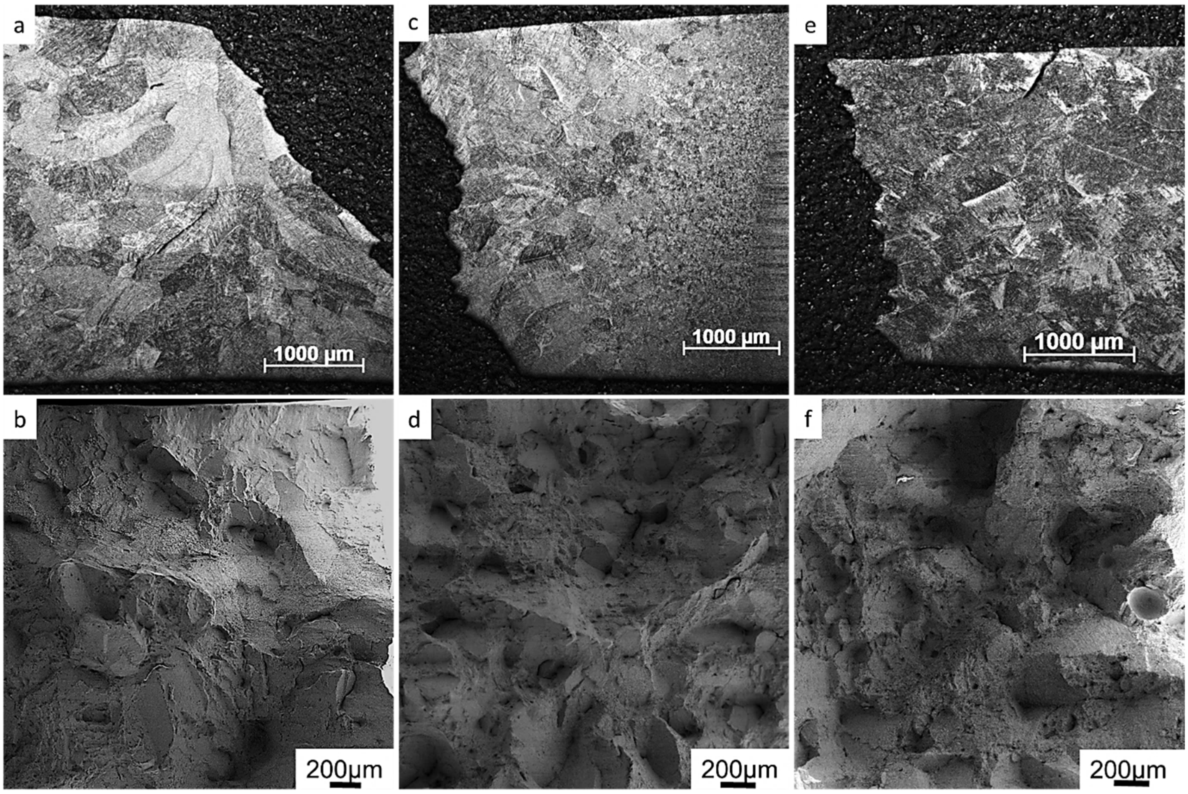

Figure 5.2. Etched side views and fracture surfaces of weld samples tensile tested at room temperate. a) and b) EBW, c) and d) LBW, and e) and f) PAW.

Figure 5.3 shows the results of LCF tests carried out at 250°C with the type of crack initiation indicated by a unique symbol. Large defects have most detrimental effect on fatigue life on all stress ranges. At high stress ranges, cracks initiate easily and surface initiations dominate. At lower stress ranges, smaller defects can act as crack initiation sites, because cracks do not initiate and grow from the surface. At room temperature, the fatigue performance was found to be more sensitive to porosity.

EBW and LBW were found to have better fatigue performance than TIG and PAW. Almost all TIG and PAW specimens had crack initiation at a pore, whereas most EBW and LBW samples had a crack initiation at a defect-free surface. Only large pores and surface pores were found to initiate cracks in EBW and LBW. The finer microstructure in EBW and LBW improves resistance to micro crack initiation which contributes to better fatigue performance and makes the welds less sensitive to porosity.

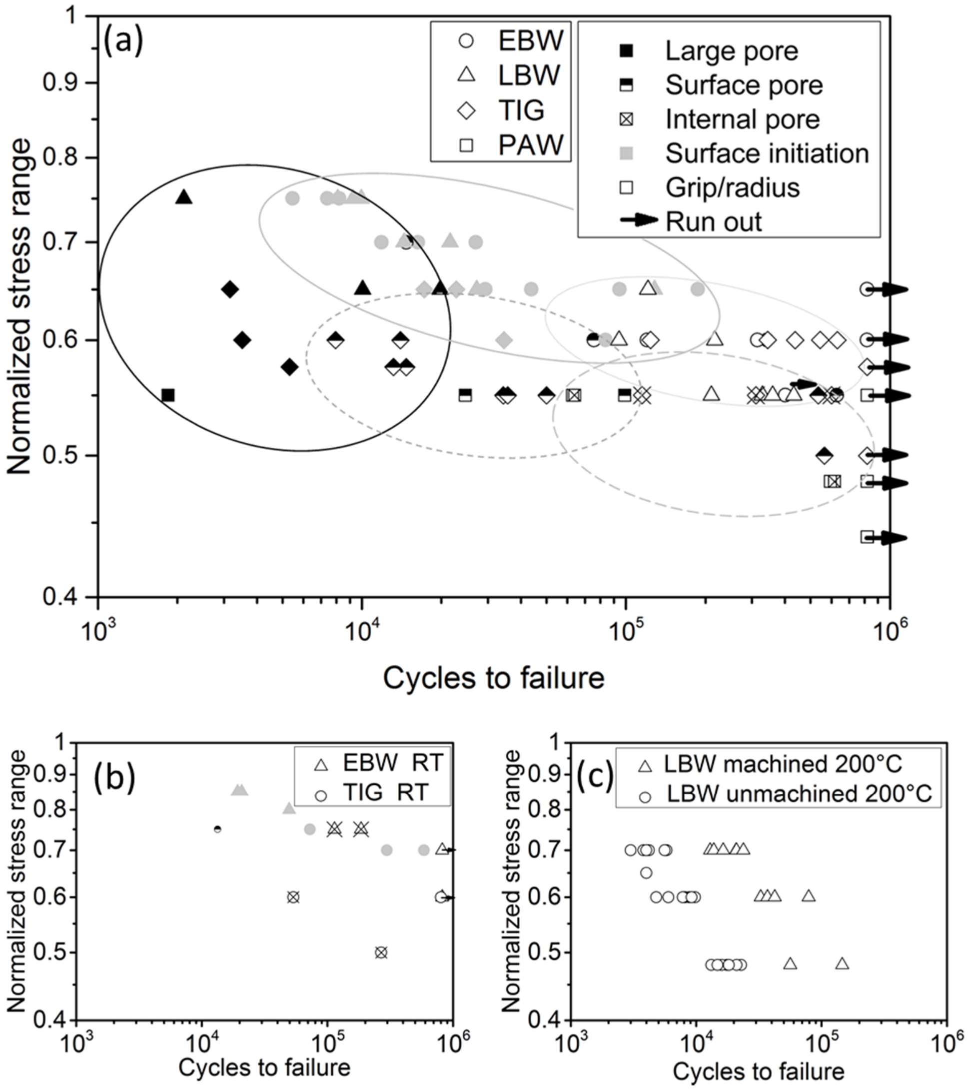

Figure 5.3. LCF results of a) welds produced by TIG, PAW, EBW and LBW at 250°C, b) EBW and TIG at room temperature, and c) the effect of weld geometry in LBW. In a) and b), the shape of the symbol indicates the welding process and the fill of the symbol indicates the type of the crack initiation.

5.3 Welding of boron alloyed Ti-6Al-4V

Addition of small amounts of boron to cast titanium alloys have shown to render a finer microstructure and improved mechanical properties. For this type of improved alloys to be fully applicable for large aerospace structural components, successful welding of such castings is essential. Addition of boron in the cast base material altered the microstructure of the LBW and TIG welds significantly as shown in Fig. 5.4. The most distinct changes that were observed were the presence of TiB particles and the refined prior-β grain size in the HAZs and FZs of the boron alloyed welds. Also, changes in α phase morphology were observed as α laths got shorter and the amount of colony type microstructure increased with increasing boron content. As shown in Fig. 5.5, the TiB particles were affected by the welding process. In the fusion zone the TiB particles were much finer and formed networks of stripes along the interdendritic regions whereas in the HAZ and base material, the TiB particles were unaffected and located along the prior-β grain boundaries.

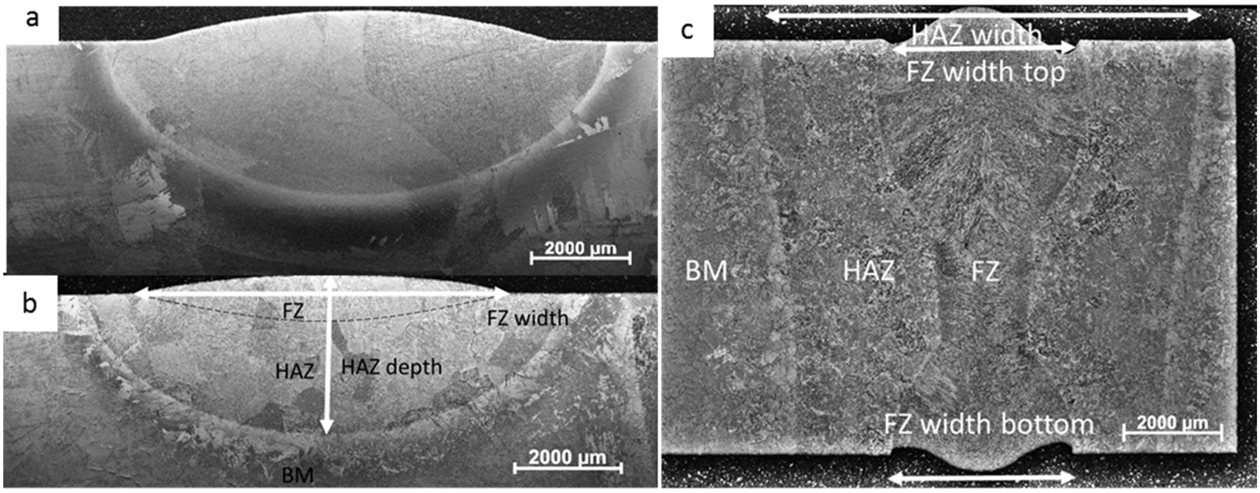

Figure 5.4. Optical micrographs of a) TIG Ti-64, b) TIG Ti-64+0.06B and c) laser weld Ti-64+0.11B.

The β-grain refinement is based on the growth restriction provided by boron as a boron-rich layer is formed around the solidifying β-grains. This boron enrichment causes a corresponding variation in the liquidus temperature, thereby leading to higher constitutional supercooling which provides an additional driving force for the nucleation of more fine β-grains ahead of the solid/liquid interface. The presence of equiaxed grains in boron alloyed titanium alloy castings implies that constitutional supercooling is more important during solidification than thermal undercooling [12].

When a steep temperature gradient is present, as in welding or additive manufacturing, columnar growth of grains tends to occur. This was observed in the FZs of boron alloyed welds. Bermingham et al. [14] explained the formation of thin elongated columnar grains by lateral solute rejection during epitaxial nucleation and growth from the base material. The presence of boron produces constitutional supercooling which restricts the lateral columnar growth allowing neighboring columnar grains to nucleate and grow. Columnar grains are also favored by the lack of potent nuclei in the melt. TiB particles that were observed in the base material and the FZ were initially dissolved in the melt and only precipitate during the last phase of solidification. Consequently, they do not affect the grain refinement during solidification. The grain boundary pinning effect of TiB particles may be important in restricting the β-grain growth when the temperature exceeds the β-transus temperature. This effect is apparent in the HAZs of boron alloyed welds where no coarsening of prior-β grains was observed.

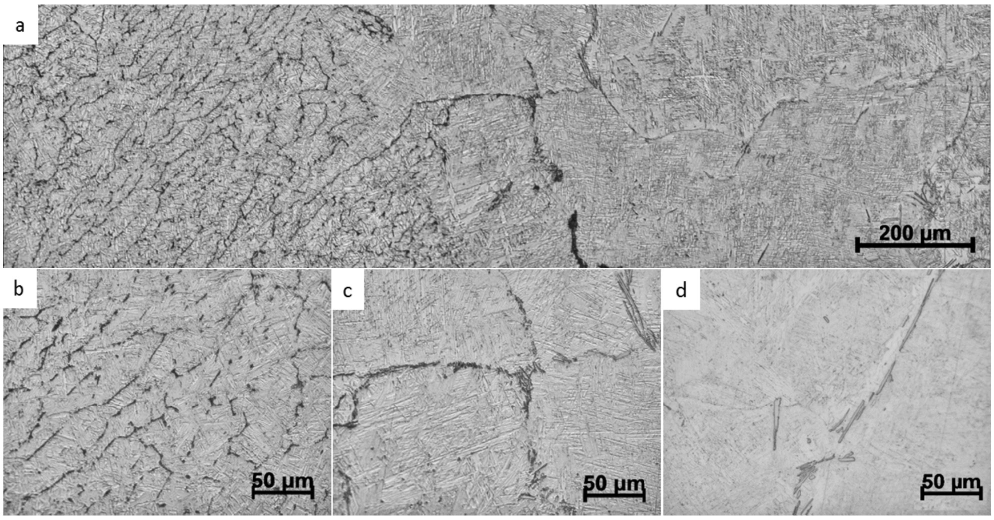

Figure 5.5. SEM images of microstructure of L-0.11B: a) FZ and HAZ, b) FZ, c) HAZ close to the fusion line, and d) HAZ.

Titanium alloys are typically very resistant to solidification cracking because of the absence of segregating elements. Addition of boron, however, may increase the risk of liquation cracking in the HAZ during welding. Close to the fusion line (Fig. 5.5c), it appears that the TiB may have partly melted/dissolved while the β-grains appear unmelted. The phase diagram for the Ti-B system [123] shows that the Ti-B eutectic has a lower melting point than pure Ti metal. This eutectic component, which segregates to the prior-β grain boundaries during solidification, could therefore risk to form a liquid film along the β-grain boundaries in the HAZ during welding. This increases the risk of liquation cracking during welding. However, no cracks were observed in this study.

The X-ray microtomography study of the laser welds revealed no significant effect of boron on the amount or size of porosity. Pores in laser welded titanium alloys are normally considered to be related with keyhole instabilities or contamination [56], [63]. However, the spatial distribution of pores was found to be different in standard grade Ti-64 (L-0B) when compared with the boron alloyed welds (L-0.06B and L-0.11B). In L-0.06B and L-0.11B, the pores were confined at the root side of the weld, whereas in L-0B, the pores were found also in the middle of the weld. Boron alloyed welds were wider than the corresponding welds of standard grade Ti-64 alloy, even though identical welding parameters were used. The face undercut was larger in L-0B than in L-0.06B and L0.11B welds. These observations are probably related to the flow of the meltpool. Boron is known to influence the melting point and solidification range of titanium alloys [12] and may have an effect on the viscosity and surface tension characteristics of the melt which therefore could influence the flow in the meltpool.

5.3.1 Prior-beta grain reconstruction

The effect of boron on prior-β grain structure was studied with EBSD analysis combined with prior-β grain reconstruction performed by the *Merengue 2* software [124]. Relatively large areas of 3 x 5 mm were mapped to acquire the overview of the base material, the HAZ and the FZ of the laser welds. A step size of 4 µm was chosen to be able to acquire maps of such large areas in timely manner. The as-measured orientation map of the α phase in a laser weld with 0.06% B is shown in Fig. 5.6a in inverse pole figure coloring. Figures 5.6 b-d show the orientation map of the numerically reconstructed β phase in laser welds with different boron contents. The step size was similar to the average size of the α colonies in the HAZ and the FZ. This means that data was not acquired from all the α colonies. The fine microstructure also resulted in a lower percentage of indexed points and lower quality of the EBSD patterns. The change in EBSD pattern quality between the base material and HAZ is illustrated by the band contrast image in Fig. 5.6f.

The reconstructed β grain map reveals the prior-β grains in the different zones. In the base material and the heat affected zone, the prior-β grains were relatively equiaxed and no significant grain growth was observed. TiB particles located in the prior-β grain boundaries seemed to restrict grain growth in the HAZ during welding. The prior-β grains in the fusion zone were narrow and elongated. The β grains nucleated and grew epitaxially from prior-β grains in the heat affected zone but there were also large number of β grains nucleating within the fusion zone. A smaller prior-β grain size in the HAZ also offers more nucleation sites for grains to grow in the FZ which contributed to the finer prior-β grain structure in the FZ. The $\{100\}_\beta$ pole figure shown in Fig 5.7e shows a weak texture in the FZ which indicates that the growth direction of the columnar grains was close to the elongation direction of the grains which is typical for competitive growth during solidification. This texture was not seen in the base material.

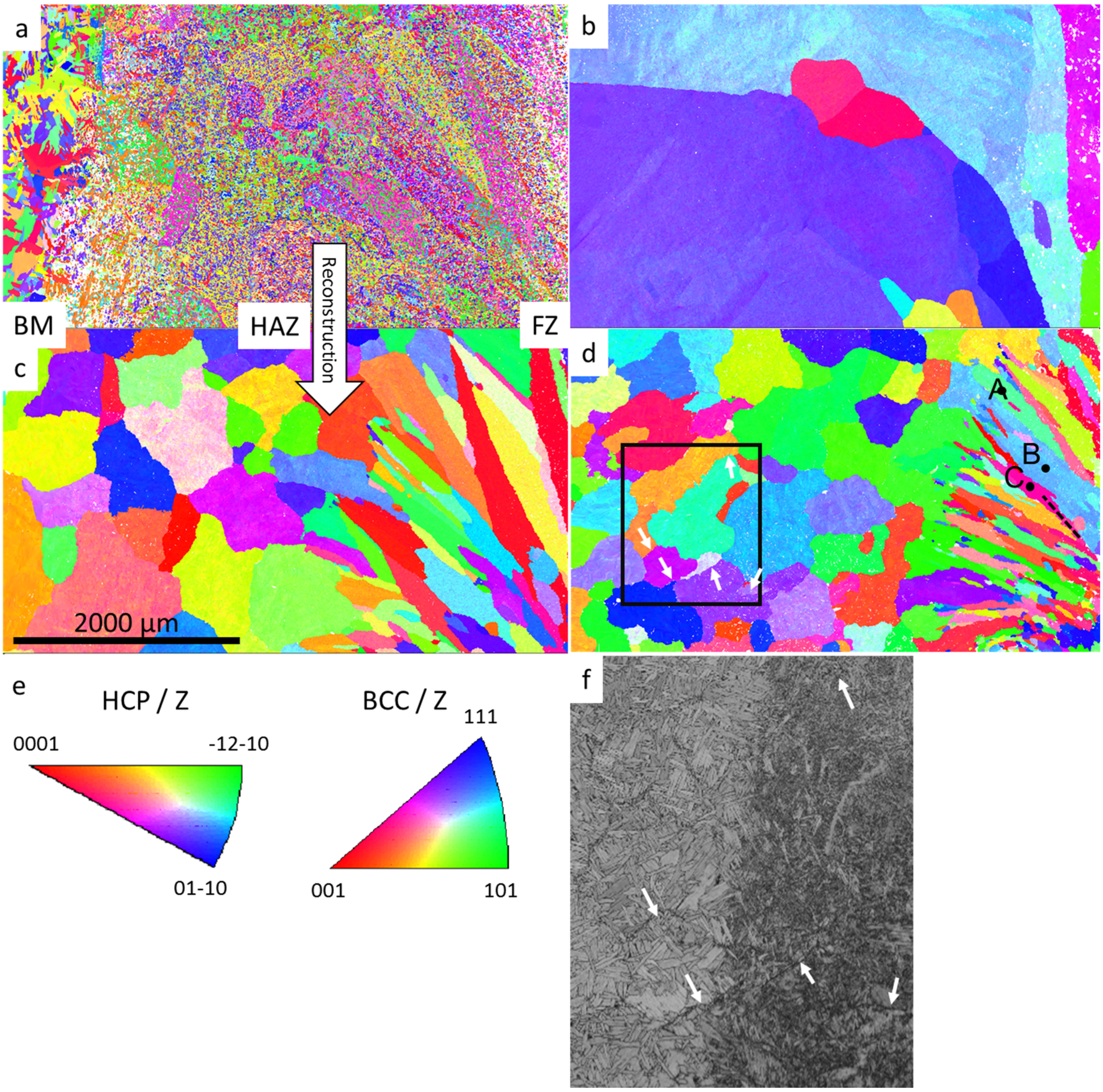

Figure 5.6. EBSD maps of a) the α phase in L-0.06B and reconstructed β phase in b) L-0B, c) L-0.06B, and d) L.0.11B. e) IPF color code for the HCP α phase and the BCC β phase and f) magnified band contrast image of BM/HAZ boundary in L-0.11B.

The reliability of the reconstruction was evaluated by comparing the band contrast image and reconstructed β grain maps. An example of the comparison is shown in Figs 5.6d and f. The reconstructed prior-β grain boundaries correspond to the locations where TiB particles were observed in the band contrast image. In the fusion zone, TiB particles were finely dispersed throughout the microstructure. Hence, validating the β grain reconstruction this way was not possible. Therefore, EBSD orientation information of selected adjacent grains A-C (indicated in Fig. 5.6) were analyzed in detail. Figure 5.7 shows pole figures of $\{0001\}_{\alpha}$, $\{011\}_{\beta}$, and the orientation map of α phase in the reconstructed β grains A-C.

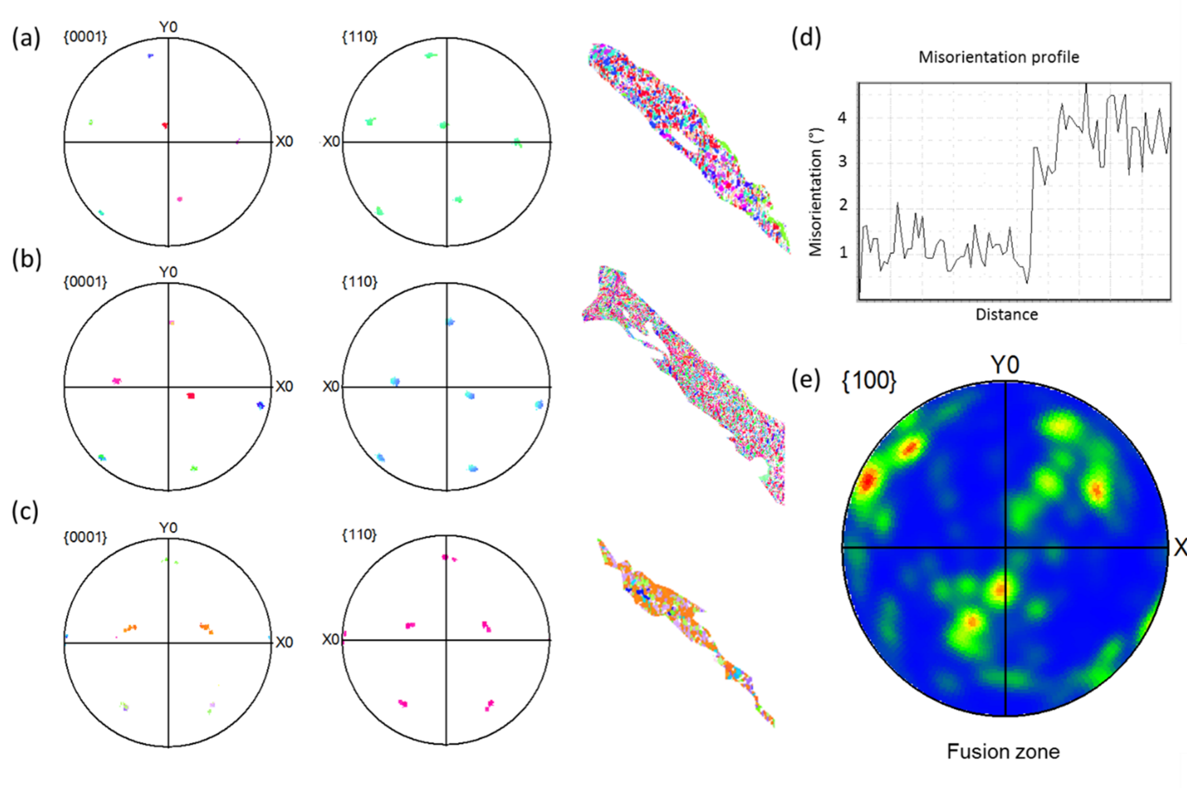

Figure 5.7. EBSD analysis of grains A-C: (a-c) $\{0001\}_{\alpha}$ pole figure, {011} pole figure of reconstructed β phase, and orientation map of α phase in grains A-C, respectively. d) Misorientation profile in the reconstructed grain C, and e) {100} pole figure of β phase in fusion zone.

As shown in Fig. 5.7, $\{0001\}_{\alpha}$ poles within each reconstructed β grain gathered into six positions in the pole figure. In β phase, there are 6 $\{011\}_{\beta}$ poles to which the $\{0001\}_{\alpha}$ poles coincide exactly according to Burgers orientation relationship. Comparison of these adjacent grains shows that the measured α variants within each grain A-C must stem from different β grains. If α variants selected in the area of an reconstructed grain originated from different β grains, the $\{0001\}_{\alpha}$ pole figure would show more than 6 poles. This is visible in grain C; there was a small shift of the projection of the $\{0001\}_{\alpha}$ poles. This is due to a low angle grain boundary which is shown in the misorientation profile (Fig. 5.7d) of reconstructed β phase measured along grain C. Overall, the reliability of the presented β grain reconstruction method appears to be good. In the base material and the heat affected zone, microstructural features revealed the prior-β grain boundaries and the reconstructed map captured these boundaries. In the fusion zone, analysis of the α variants stemming from adjacent β grains showed that β grains were correctly reconstructed.

5.4 Effect of material variation in porosity in laser welding

In laser welding, the formation of porosity is mainly attributed to instabilities related to the keyhole. Several studies have shown that keyhole instability can lead to metal vapor or inert gas getting trapped in the weld metal [57], [68], [70]. However, significant variations between material batches in terms of porosity formation have been observed. Therefore, in this study, a blocked 2^k factorial study was designed in order to determine the effect of material variation and welding parameters on weld metal porosity. The factorial design was replicated in four material batches with differing chemical compositions. The 3 key process variables; welding speed, average power and pulse length, and the appropriate range for these variables were chosen based on previous experience. 11 bead-on-plate welds were deposited on each batch of material and the welds were characterized in terms of microstructure, weld geometry and weld metal porosity. The material batches were characterized in detail to explain the batch variation in the amount of weld metal porosity.

Characterization of the material batches showed differences in chemical composition, hardness and homogeinity of the microstructure. The microstructure of all material batches was fully equiaxed. Some of the batches showed differing degrees of banding. The Vickers hardness of material batches was varying between 323 HV and 354 HV. The chemical compositions of the material batches (BM) and selected welds are shown in Table 5.1.

Table 5.1. Chemical compositions of different material batches and selected welds (in wt-%).

Batch/ Run	Al [%]	V [%]	Fe [%]	C [%]	N [%]	O [%]	H [ppm]	Ti
1/BM	6.08	3.88	0.19	0.008	0.010	0.14	38	Bal.
2/BM	5.92	4.04	0.16	0.016	0.008	0.17	28	Bal.
3/BM	6.23	3.82	0.17	0.009	0.012	0.14	43	Bal.
4/BM	6.13	3.93	0.20	0.011	0.009	0.16	28	Bal.
1/CP				0.009	0.006	0.14	31	
1/CP				0.012	0.006	0.14	39	
2/CP				0.017	0.008	0.16	28	
2/HP				0.020	0.006	0.14	20	

The porosity in the welds was characterized using X-ray radiography. Figure 5.8 shows radiographs of welds in batches 1 and 2 produced with same welding parameters. The porosity was classified in three categories, i.e. large pores, small pores and chain porosity. The diameters of observed porosity were summed up to cumulative length of porosity which was used as a measure of amount of porosity.

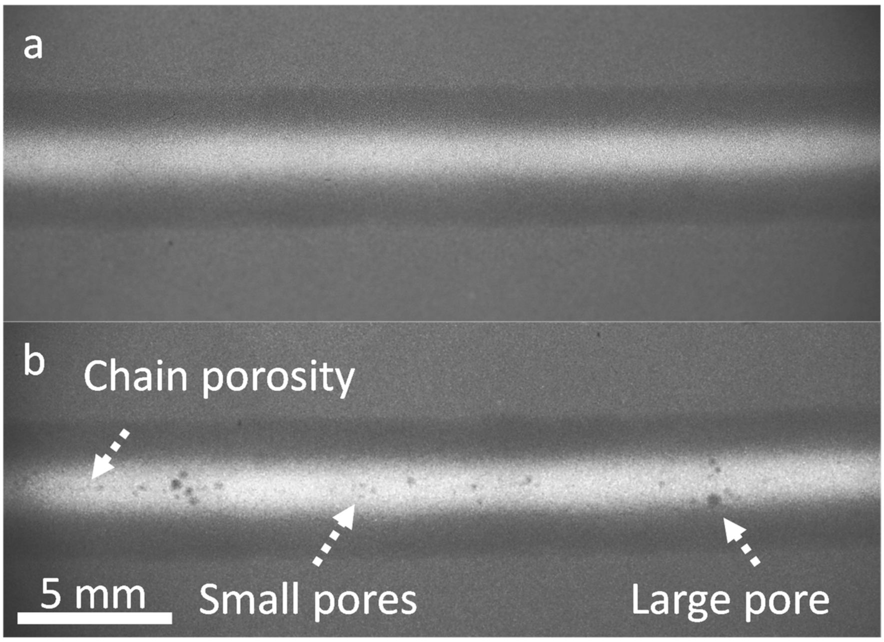

Figure 5.8. X-ray radiograph of a weld in a) batch 1 and b) batch 2 produced with the same weld parameters.

Figure 5.9 shows the amount of porosity in the 3 DOE center point welds in each batch. It shows that batches 2 and 4 were significantly more susceptible to formation of porosity than the batches 1 and 3. The variance in amount of porosity within the batches was smaller than the variance between the batches.

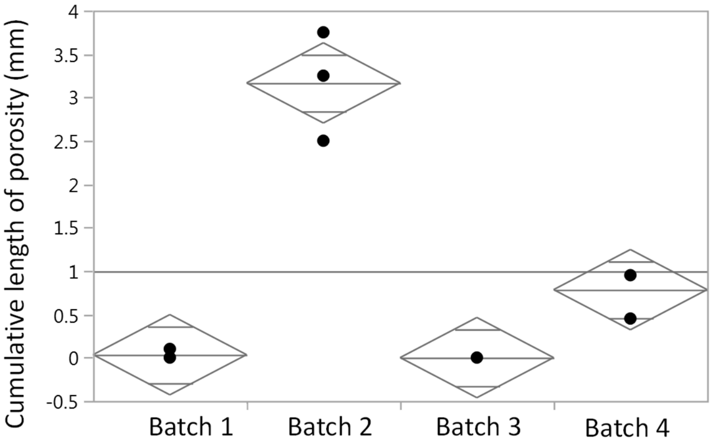

Figure 5.9. Cumulative length of porosity in the center point welds in the 4 material batches.

Welding parameters had also a significant effect on amount of porosity. Welding speed, laser pulse length and combined effect of welding speed and pulse length were found to be the most significant factors along with the material batch. Figure 5.10 shows response surfaces for amount of porosity for batches 1 and 2. The response in amount of porosity to change of welding parameters was found to be similar in each batch. However, the level of response varies significantly. The amount of porosity could be minimized in all the batches with optimization of welding parameters. In terms of porosity, acceptable welds according to AWS D17.1 specification [125] could be obtained in all material batches.

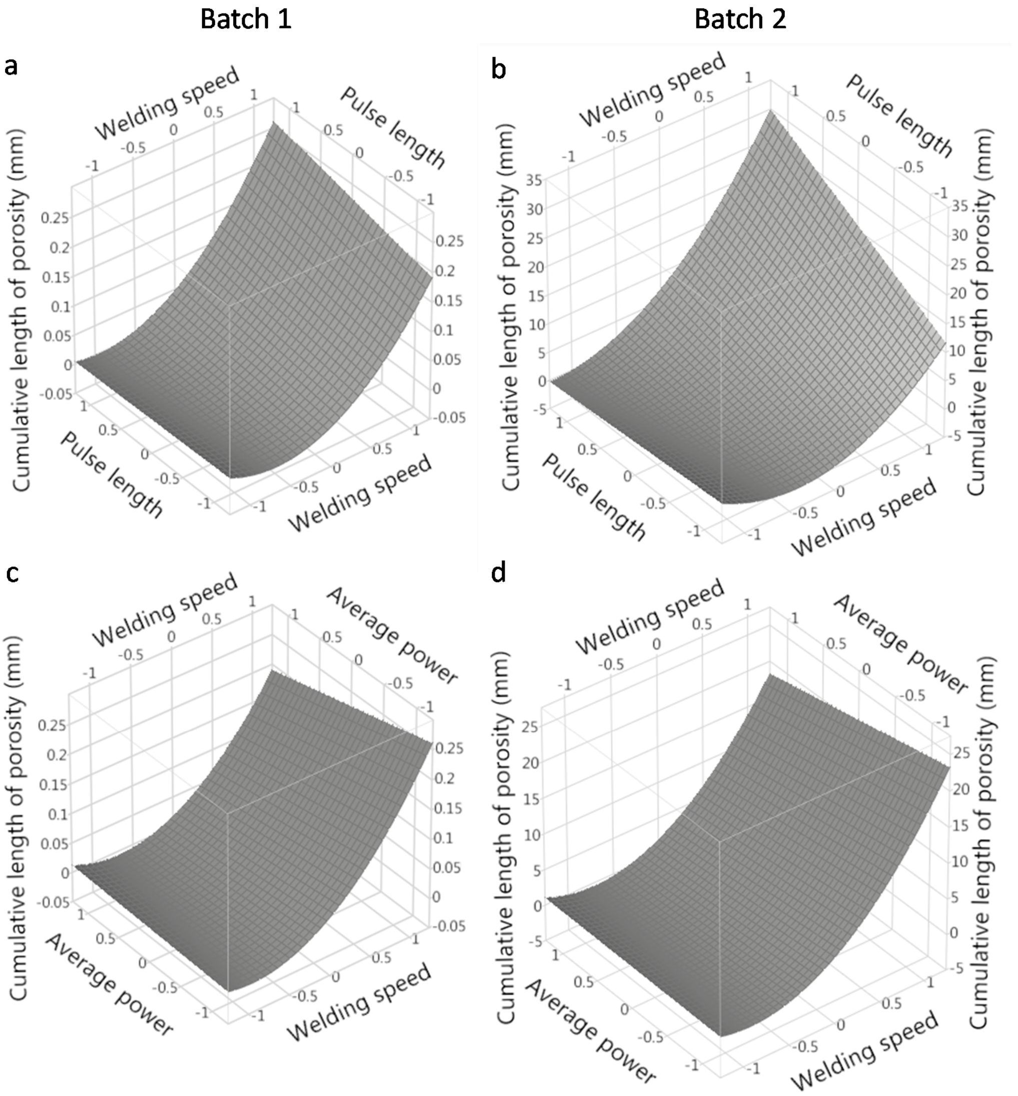

Figure 5.10. Response surfaces for cumulative length of porosity for given power level 0 (a and b), and for given pulse length level 0 (c and d) in batches 1 and 2, respectively.

To study the sources of the batch-to-batch variation in porosity, the 4 material batches were characterized in terms of chemical composition, microstructure and hardness. Figure 5.11 shows the amount of different alloying elements in relation to the accumulated length of porosity in the center point welds. The material batches with most hydrogen and nitrogen had the lowest amount of weld metal porosity while the material batches having increased amount of carbon and oxygen showed increased amount of weld metal porosity. Table 5.1 shows the chemical compositions of center point welds in batches 1 and 2 (CP) and the composition in a weld with high amount of porosity in batch 2 (HP). Contamination of the weld metal was not observed. All the welds appeared to have a slight increase in carbon content compared to the base materials whereas the amount of O, N, and H was at the same level or slightly lower than in the base materials. The change in all the welds was similar. The amounts of C, O, N and H in the weld metal were within the AMS 4911N specification.

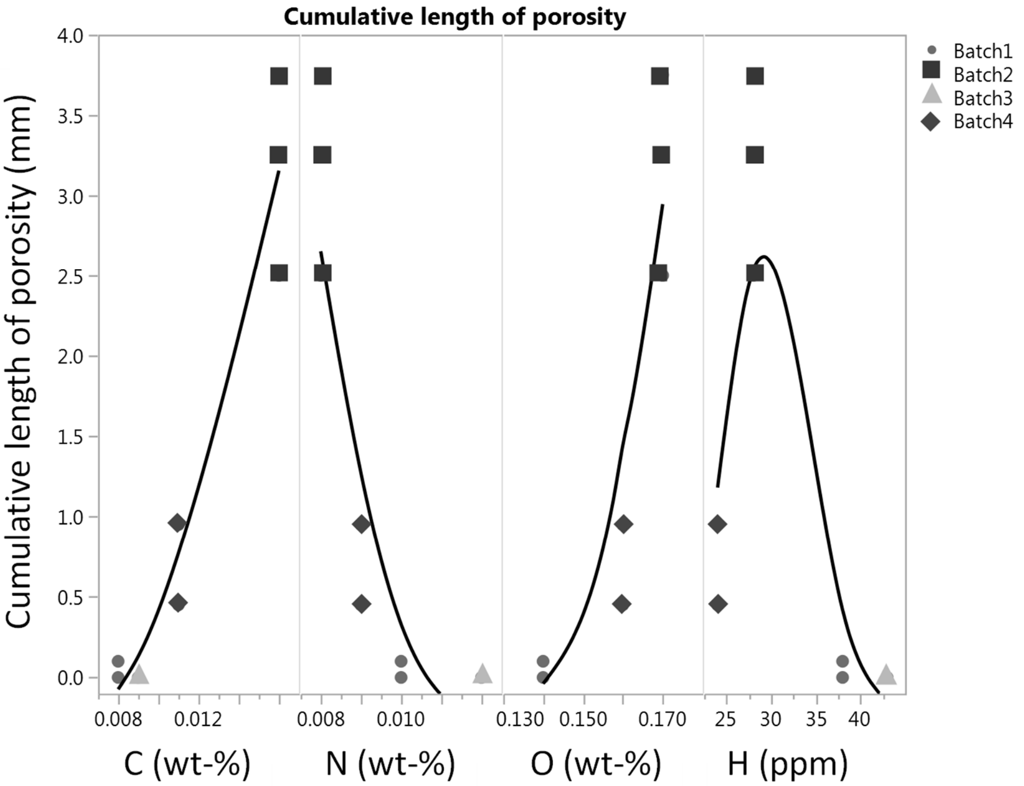

Figure 5.11. Cumulative length of porosity in central point welds in relation to the chemical composition of the base material. There are 3 center points in each batch, but some of the data points are overlapping.

Partial least squares (PLS) analysis showed that the most important variables were welding speed and amount of carbon, together with banding of microstructure and amount of oxygen. Increased amount of hydrogen did not increase the amount of porosity. Base material hardness and amount of β phase did not have an effect either. PLS showed that some of the factors were not independent. The amount of carbon and oxygen were correlated in the batches used in the present study. Hence, it is not possible to separate their individual effects based on this data.

It was shown that there is significant batch-to-batch variation in amount of porosity in laser welding of Ti-6Al-4V. However, it was difficult to point out an exact source of the batch-to-batch variation in formation of porosity. Typically in laser welding, keyhole fluctuations are the main cause of porosity. The variation in the base material chemical composition, surface condition or local variation (e.g. banding) may affect the surface tension, viscosity or reflectivity of the meltpool that affect the force balance in the keyhole. Evaporating elements and surface contaminations may also be important. Further studies are required to identify the sources of batch-to-batch variation in terms of porosity.

5.5 Conclusions

The aim of the work was to study what kind of microstructures and defects are formed in welding of Ti-6Al-4V with different welding processes and how these aspects affect the mechanical properties of the welds. Furthermore, the influence of chemical composition of the alloy on the formation of microstructures and defects was investigated. The study showed that TIG, PAW, LBW and EBW are all processes capable of creating high quality fusion welded joints in titanium alloys. The welds had different microstructures and different populations of defects in terms of their size and distribution. The welds produced by TIG and PAW had wider weld zones, coarser prior β grain structure and coarser intragranular microstructure. EBW and LBW welds were narrow and had very fine acicular intragranular microstructure. Fractographic investigation and X-ray microscopy showed that TIG and LBW had more porosity with larger size than EBW and PAW.

The differences in the microstructures and defect distribution were found to have an effect on the mechanical properties. The finer microstructure in EBW and LBW contributed to higher tensile strength and tensile ductility of these welds. The finer microstructure has also a higher resistance to micro crack initiation and micro crack growth which contributed to better fatigue performance of EBW and LBW welds. The fatigue results showed large scatter and fractographic investigation revealed that presence of large pores and surface pores decreased the fatigue life significantly. The fatigue performance of EBW and LBW welds seemed to be less sensitive to porosity, as most samples had crack initiation at the surface of the sample. On the contrary, welds produced by TIG and PAW had a crack initiation almost always at a pore. Small internal pores were more detrimental to fatigue life at room temperature than at elevated temperatures.

The alloy composition had a significant influence on the microstructure of the welds and the formation of defects. A small boron addition refined the grain size significantly and rendered narrow columnar grains in the fusion zone. A significant feature of the welds in boron alloyed material was the presence of TiB particles. In the cast base material, the TiB particles were located in the prior-β grain boundaries restricting the grain growth in the HAZ. In the fusion zones of the welds, TiB particles formed networks of stripes along the interdendritic regions. The TiB particles were affected by the welding process. In the fusion zone and HAZ close to the fusion line, the size of TiB particles was smaller than in the base material indicating that TiB particles were dissolved during welding. This may increase the risk of liquation cracking in the HAZ of welds in boron alloyed titanium alloys. TiB particles act as nucleation sites for α phase leading to decreased length of α laths when boron was added. The width of the FZ and the distribution of porosity were affected by boron addition which may indicate that boron affects the melt pool flow during welding. EBSD combined with prior-β grain reconstruction was an effective method to reveal the prior-β grain structure in the base material, the HAZ and the FZ. The original EBSD map was measured at low magnification and relatively large step size in comparison to the size of the α micro-constituents. The fine microstructure together with low magnification resulted in a relatively low indexing rate in the fusion zone and heat affected zone. Even with the low indexing rate, the prior-β grain reconstruction could be performed successfully with good reliability.

A significant batch-to-batch variation in formation of porosity was observed in laser welding of Ti-6Al-4V. It was found that most significant factors affecting formation of porosity were the material batch, pulse length and welding speed. Multivariate analysis showed that out of the base material properties, the amount of carbon and oxygen and banding of microstructure were most important variables affecting porosity. Amount of hydrogen, fraction of β phase or hardness of the base material were not found to affect formation of porosity. Formation of porosity could be minimized in all material batches by optimizing the welding parameters.

6. Suggestions for future work

Addition of small amounts of boron to cast Ti-6Al-4V alloy has shown to render in a finer microstructure in the weld zones. However, for such an improved alloy to be widely applicable for aerospace structural components, further studies are required. The mechanical properties and the effect of heat treatments need to be characterized in more detail. The boron rich Ti-TiB eutectic along the prior-β grain boundaries has lower melting point therefore increasing the risk of liquation cracking. The liquation cracking susceptibility of boron alloyed titanium alloys should be further evaluated.

A significant batch-to-batch variation in amount of porosity was observed between material batches in laser welding of Ti-6Al-4V. Because of the complex nature involved where several variables influence the formation of porosity, it was difficult to point out an exact source and mechanism for the batch-to-batch variation. More experimental data is needed to confirm if C and O are the cause of porosity. Keyhole monitoring could be used to confirm if the porosity is related to keyhole instabilities. Furthermore, most simulation efforts are being performed with nominal material composition and material data. Small changes in impurity levels may change the properties of the melt which is another area where further work is required.

7. Acknowledgements

I would like to thank and express my sincere gratitude to my examiner and supervisor Professor Uta Klement and supervisor Professor Robert Pederson for their guidance, patience and encouragement in the last five years. Your professional and personal support has been invaluable for the development of this work.

I would like to thank our research engineers: Dr. Eric Tam, Dr. Yiming Yao, Mr. Lars Hammar and Mr. Roger Sagdal for all the practical support. Special thanks goes to Dr. Kenneth Hamberg who introduced me to the world of fatigue fractures and metallographic preparation of titanium alloys. I would also like to acknowledge GKN Aerospace Engine Systems for providing materials, welding experiments, mechanical testing, and expertise which the current thesis is based on. NFFP (the Swedish National Program for Aeronautical Technology) is acknowledged for financial support of this PhD project.

I would like to thank my former and current colleagues at the Department of Industrial and Materials Science for creating a friendly and motivating working environment. I would like to thank all my friends for making my stay in Sweden unforgettable and the friends in Finland, I will not forget you.

My family and parents, I would not be here without you.

References

[1] R. R. Boyer, “An overview on the use of titanium in the aerospace industry,” *Mater. Sci. Eng. A*, vol. 213, no. 1–2, pp. 103–114, Aug. 1996.

[2] G. W. Meetham, Ed., *The Development of Gas Turbine Materials*. Dordrecht: Springer Netherlands, 1981.

[3] F. H. S. Froes and M. A. Imam, “Cost Affordable Developments in Titanium Technology and Applications,” *Key Eng. Mater.*, vol. 436, no. May, pp. 1–11, 2010.

[4] H. Beladi, Q. Chao, and G. S. Rohrer, “Variant selection and intervariant crystallographic planes distribution in martensite in a Ti-6Al-4V alloy,” *Acta Mater.*, vol. 80, pp. 478–489, 2014.

[5] W. G. Burgers, “On the process of transition of the cubic-body-centered modification into the hexagonal-close-packed modification of zirconium,” *Physica*, vol. 1, no. 7–12, pp. 561–586, 1934.

[6] M. J. Donachie, *Titanium A Technical Guide*, 2nd ed. Materials Park, Ohio: ASM International, 2000.

[7] G. Lütjering and J. C. William, *Titanium*. Springer-Verlag Berlin Heidelberg New York, 2003.

[8] M. Peters and C. Leyens, *Titanium and Titanium Alloys - Fundamentals and Applications*, vol. 1. Wiley-VCH, 2003.

[9] R. Pederson, R. Gaddam, and M.-L. Antti, “Microstructure and mechanical behavior of cast Ti-6Al-4V with addition of boron,” *Cent. Eur. J. Eng.*, vol. 2, no. 3, pp. 347–357, 2012.

[10] G. Singh, R. Gaddam, V. Petley, R. Datta, R. Pederson, and U. Ramamurty, “Strain-controlled fatigue in B-modified Ti-6Al-4V alloys,” *Scr. Mater.*, vol. 69, no. 9, pp. 698–701, 2013.

[11] G. Singh, D. V. V Satyanarayana, R. Pederson, R. Datta, and U. Ramamurty, “Enhancement in creep resistance of Ti-6Al-4V alloy due to boron addition,” *Mater. Sci. Eng. A*, vol. 597, pp. 194–203, 2014.

[12] S. Roy, S. Suwas, S. Tamirisakandala, D. B. Miracle, and R. Srinivasan, “Development of solidification microstructure in boron-modified alloy Ti-6Al-4V-0.1B,” *Acta Mater.*, vol. 59, no. 14, pp. 5494–5510, 2011.

[13] S. Tamirisakandala, R. B. Bhat, J. S. Tiley, and D. B. Miracle, “Grain refinement of cast titanium alloys via trace boron addition,” *Scr. Mater.*, vol. 53, no. 12, pp. 1421–1426, 2005.

[14] M. J. Bermingham, D. Kent, H. Zhan, D. H. StJohn, and M. S. Dargusch, “Controlling the microstructure and properties of wire arc additive manufactured Ti–6Al–4V with trace boron additions,” *Acta Mater.*, vol. 91, pp. 289–303, 2015.

[15] I. Maxwell and A. Hellawell, “A simple model for grain refinement during solidification,” *Acta Metall.*, vol. 23, no. 2, pp. 229–237, 1975.

[16] M. J. Bermingham, S. D. McDonald, M. S. Dargusch, and D. H. St.John, “Grain-refinement mechanisms in titanium alloys,” *J. Mater. Res.*, vol. 23, no. 1, pp. 97–104, 2008.

[17] O. M. Ivasishin, R. V. Teliovych, V. G. Ivanchenko, S. Tamirisakandala, and D. B. Miracle, “Processing, Microstructure, Texture, and Tensile Properties of the Ti-6Al-4V-1.55B Eutectic Alloy,” *Metall. Mater. Trans. A*, vol. 39, no. 2, pp. 402–416, 2008.

[18] R. Srinivasan and S. Tamirisakandala, “Influence of trace boron addition on the directional solidification characteristics of Ti–6Al–4V,” *Scr. Mater.*, vol. 63, no. 12, pp. 1244–1247, 2010.

[19] Z. Mahbooba, H. West, O. Harrysson, A. Wojcieszynski, R. Dehoff, P. Nandwana, and T. Horn, “Effect of Hypoeutectic Boron Additions on the Grain Size and Mechanical Properties of Ti-6Al-4V Manufactured with Powder Bed Electron Beam Additive Manufacturing,” *Jom*, vol. 69, no. 3, pp. 472–478, 2017.

[20] S. Tolvanen, R. Pederson, and U. Klement, “Microstructure and Porosity of Laser Welds in Cast Ti-6Al-4V with Addition of Boron,” *Metall. Mater. Trans. A Phys. Metall. Mater. Sci.*, vol. 49, no. 5, pp. 1–9, 2018.

[21] M. J. Bermingham, S. D. Mcdonald, M. S. Dargusch, and D. H. Stjohn, “Microstructure of Cast Titanium Alloys,” *Mater. Forum*, vol. 31, pp. 84–89, 2007.

[22] J. Zhu, A. Kamiya, T. Yamada, W. Shi, and K. Naganuma, “Influence of boron addition on microstructure and mechanical properties of dental cast titanium alloys,” *Mater. Sci. Eng. A*, vol. 339, no. 1–2, pp. 53–62, 2003.

[23] J. H. Luan, Z. B. Jiao, L. Heatherly, E. P. George, G. Chen, and C. T. Liu, “Effects of boron on the fracture behavior and ductility of cast Ti-6Al-4V alloys,” *Scr. Mater.*, vol. 100, pp. 90–93, 2015.

[24] S. A. Mantri, T. Torgerson, E. Ivanov, T. W. Scharf, and R. Banerjee, “Effect of Boron Addition on the Mechanical Wear Resistance of Additively Manufactured Biomedical Titanium Alloy,” *Metall. Mater. Trans. A Phys. Metall. Mater. Sci.*, vol. 49, no. 3, pp. 806–810, 2018.

[25] I. Sen, K. Gopinath, R. Datta, and U. Ramamurty, “Fatigue in Ti – 6Al – 4V – B alloys,” *Acta Mater.*, vol. 58, pp. 6799–6809, 2010.

[26] ASM International: Handbook Committee, *ASM Handbook, Volume 6A: Welding Fundamentals and Processes*. ASM International, 1993.

[27] S. Katayama, *Handbook of Laser Welding*, vol. 9, no. 2012. Philadelphia, USA: Woodhead Publishing, 2013.

[28] K. Weman, *Welding processes handbook*. Philadelphia, PA: Woodhead Pub, 2012.

[29] C. S. Wu, L. Wang, W. J. Ren, and X. Y. Zhang, "Plasma arc welding: Process, sensing, control and modeling," *J. Manuf. Process.*, vol. 16, no. 1, pp. 74–85, 2014.

[30] C. L. Jenney and A. O'Brien, *Welding handbook*, 9th ed. Miami: American Welding Society, 2001.

[31] W. Haynes, D. Lide, and T. Bruno, *CRC Handbook of Chemistry and Physics, 94th Edition*, 94th ed. Boca Raton, FL: Taylor & Francis Group, 2013.

[32] J. Blackburn, *Laser welding of metals for aerospace and other applications*. Woodhead Publishing Limited, 2011.

[33] H. G. Fan, H. L. Tsai, and S. J. Na, "Heat transfer and fluid flow in a partially or fully penetrated weld pool in gas tungsten arc welding," *Int. J. Heat Mass Transf.*, vol. 44, pp. 417–428, 2000.

[34] A. Kaplan, "Keyhole Welding: The Solid and Liquid Phases," Springer, Cham, 2017, pp. 89–112.

[35] R. Fabbro and K. Chouf, "Keyhole modeling during laser welding," *J. Appl. Phys.*, vol. 87, no. 9, p. 4075, Apr. 2000.

[36] S. Kou, *Welding Metallurgy Second Edition*. Hoboken, NJ, 2003.

[37] S. A. David and J. M. Vitek, "Correlation between solidification parameters and weld microstructures," *Int. Mater. Rev.*, vol. 34, no. 1, pp. 213–245, Jan. 1989.

[38] J. N. DuPont, "Fundamentals of Weld Solidification," *ASM Handb. Vol 6, Welding, Brazing Solder.*, vol. 6, pp. 96–114, 2011.

[39] K. E. Easterling, *Introduction to the physical metallurgy of welding*. Butterworth Heinemann, 1992.

[40] G. Q. Wang, Z. B. Zhao, B. B. Yu, J. R. Liu, Q. J. Wang, J. H. Zhang, R. Yang, and J. W. Li, "Effect of base material on microstructure and texture evolution of a Ti-6Al-4V electron-beam welded joint," *Acta Metall. Sin. (English Lett.*, vol. 30, no. 5, pp. 499–504, 2017.

[41] K. K. Murthy, N. B. Potluri, and S. Sundaresan, "Fusion zone microstructure and fatigue crack growth behaviour in Ti-6Al-4V alloy weldments," *Mater. Sci. Technol.*, vol. 13, no. June, pp. 503–510, Jun. 1997.

[42] T. Ahmed and H. J. Rack, “Phase transformations during cooling in alpha + beta titanium alloys,” *Mater. Sci. Eng. A*, vol. 243, pp. 206–211, 1998.

[43] S. K. Kar, “Modeling of mechanical properties in alpha/beta-titanium alloys,” The Ohio State University, 2005.

[44] A. B. Short, “Gas tungsten arc welding of α + β titanium alloys: a review,” *Mater. Sci. Technol.*, vol. 25, no. 3, pp. 309–324, Mar. 2009.

[45] F. Fomin, V. Ventzke, F. Dorn, N. Levichev, and N. Kashaev, “Effect of Microstructure Transformations on Fatigue Properties of Laser Beam Welded Ti□6Al□4V Butt Joints Subjected to Postweld Heat Treatment,” *Study Grain Bound. Character*, 2017.

[46] F. X. Gil Mur, D. Rodríguez, and J. a. Planell, “Influence of tempering temperature and time on the α′-Ti-6Al-4V martensite,” *J. Alloys Compd.*, vol. 234, no. 2, pp. 287–289, 1996.

[47] K. K. Murthy and S. Sundaresan, “Fracture toughness of Ti-6Al-4V after welding and postweld heat treatment.pdf,” *Weld. J.*, vol. 76, no. 2, pp. 81–91, 1997.

[48] X. J. Cao, G. Debaecker, M. Jahazi, S. Marya, J. Cuddy, and A. Birur, “Effect of Post-Weld Heat Treatment on Nd: YAG Laser Welded Ti-6Al-4V Alloy Quality,” *Mater. Sci. Forum*, vol. 638–642, pp. 3655–3660, 2010.

[49] A. S. H. Kabir, X. Cao, J. Gholipour, P. Wanjara, J. Cuddy, A. Birur, and M. Medraj, “Effect of Postweld Heat Treatment on Microstructure, Hardness, and Tensile Properties of Laser-Welded Ti-6Al-4V,” *Metall. Mater. Trans. A*, vol. 43, no. 11, pp. 4171–4184, Jun. 2012.

[50] T. Matsumoto, N. Fukuda, Y. Kondo, A. Ohmori, K. Inoue, and Y. Arata, “Study on prevention of welding defects in high power CO2 laser materials processing,” *J. Laser Appl.*, vol. 11, no. 6, p. 258, 1999.

[51] L. S. Smith and M. F. Gittos, “A review of Weld Metal Porosity and Hydride Cracking in Titanium and Its Alloys, report 658,” The Welding Institute, 1998.

[52] T. Khaled, “An Investigation of Pore Cracking in Titanium Welds,” *Weld*, vol. 3, no. June, 1994.

[53] M. M. Alam, J. Powell, a. F. H. Kaplan, J. Tuominen, P. Vuoristo, J. Miettinen, J. Poutala, J. Näkki, J. Junkala, and T. Peltola, “Surface pore initiated fatigue failure in laser clad components,” *J. Laser Appl.*, vol. 25, no. 3, p. 032004, 2013.

[54] J. Schijve, *Fatigue of Structures and Materials*. Springer Science+Business Media, B.V., 2009.

[55] F. Karimzadeh, M. Salehi, A. Saatchi, and M. Meratian, "Effect of microplasma arc welding process parameters on grain growth and porosity distribution of thin sheet Ti6Al4V alloy weldment," *Mater. Manuf. Process.*, vol. 20, no. 2, pp. 205–219, 2005.

[56] J. Huang, "The characterisation and modelling of porosity formation in electron beam welded titanium alloys," The University of Birmingham, 2011.

[57] A. Matsunawa, M. Mizutani, S. Katayama, and N. Seto, "Porosity formation mechanism and its prevention in laser welding," *Weld. Int.*, vol. 17, no. 6, pp. 431–437, Jun. 2003.

[58] V. . Lakomski and N. . Kalinyuk, "The solubility of hydrogen in liquid titanium," *Autom. Weld.*, vol. 16, no. 9, pp. 28–32, 1963.

[59] N. Gouret, G. Dour, B. Miguet, E. Ollivier, and R. Fortunier, "Assessment of the Origin of Porosity in Electron-Beam-Welded TA6V Plates," *Metall. Mater. Trans. A*, vol. 35, no. March, pp. 879–889, 2004.

[60] C. Panwisawas, B. Perumal, R. M. Ward, N. Turner, R. P. Turner, J. W. Brooks, and H. C. Basoalto, "Keyhole formation and thermal fluid flow-induced porosity during laser fusion welding in titanium alloys: Experimental and modelling," *Acta Mater.*, vol. 126, pp. 251–263, 2017.

[61] A. Matsunawa, J.-D. Kim, N. Seto, M. Mizutani, and S. Katayama, "Dynamics of keyhole and molten pool in laser welding," *J. Laser Appl.*, vol. 10, no. 6, p. 247, 1998.

[62] A. F. H. Kaplan, M. Mizutani, and S. Katayama, "On the Mechanism of pore formation during keyhole laser spot welding," in *Proceedings of the SPIE*, 2003, vol. 4831, pp. 186–191.

[63] J. E. Blackburn, "Understanding porosity formation and prevention when welding titanium alloys with 1 μm wavelength laser beams," The University of Manchester, 2011.

[64] J. L. Huang, N. Warnken, J. C. Gebelin, M. Strangwood, and R. C. Reed, "On the mechanism of porosity formation during welding of titanium alloys," *Acta Mater.*, vol. 60, no. 6–7, pp. 3215–3225, 2012.

[65] S. Pang, W. Chen, and W. Wang, "A Quantitative Model of Keyhole Instability Induced Porosity in Laser Welding of Titanium Alloy," *Metall. Mater. Trans. A*, vol. 45, no. 6, pp. 2808–2818, Feb. 2014.

[66] A. F. H. Kaplan, M. Mizutani, S. Katayama, and A. Matsunawa, "Unbounded keyhole collapse and bubble formation during pulsed laser interaction with liquid zinc," *J. Phys. D. Appl. Phys.*, vol. 35, no. 11, pp. 1218–1228, Jun. 2002.

[67] T. Klein, M. Vicanek, and G. Simon, “Forced oscillations of the keyhole in penetration laser beam welding,” *J. Phys. D. Appl. Phys.*, vol. 29, no. 2, pp. 322–332, 1996.

[68] C. Panwisawas, Y. Sovani, R. P. Turner, J. W. Brooks, H. C. Basoalto, and I. Choquet, “Modelling of thermal fluid dynamics for fusion welding,” *J. Mater. Process. Technol.*, vol. 252, no. September 2017, pp. 176–182, 2018.

[69] L. Huang, X. Hua, D. Wu, and F. Li, “Numerical study of keyhole instability and porosity formation mechanism in laser welding of aluminum alloy and steel,” *J. Mater. Process. Technol.*, vol. 252, no. September 2017, pp. 421–431, 2018.

[70] J. Zhou and H.-L. Tsai, “Porosity Formation and Prevention in Pulsed Laser Welding,” *J. Heat Transfer*, vol. 129, no. 8, p. 1014, 2007.

[71] X. Cao, A. S. H. Kabir, P. Wanjara, J. Gholipour, A. Birur, J. Cuddy, and M. Medraj, “Global and Local Mechanical Properties of Autogenously Laser Welded Ti-6Al-4V,” *Metall. Mater. Trans. A*, vol. 45, no. 3, pp. 1258–1272, Nov. 2013.

[72] H. Zhao, W. Niu, B. Zhang, Y. Lei, M. Kodama, and T. Ishide, “Modelling of keyhole dynamics and porosity formation considering the adaptive keyhole shape and three-phase coupling during deep-penetration laser welding,” *J. Phys. D. Appl. Phys.*, vol. 44, no. 48, p. 485302, Dec. 2011.

[73] J. Ahn, L. Chen, C. M. Davies, and J. P. Dear, “Parametric optimisation and microstructural analysis on high power Yb-fibre laser welding of Ti–6Al–4V,” *Opt. Lasers Eng.*, vol. 86, pp. 156–171, 2016.

[74] B. Chang, C. Allen, J. Blackburn, P. Hilton, and D. Du, “Fluid Flow Characteristics and Porosity Behavior in Full Penetration Laser Welding of a Titanium Alloy,” *Metall. Mater. Trans. B*, 2014.

[75] J. Blackburn, C. Allen, P. Hilton, and L. Li, “Nd:YAG laser welding of titanium alloys using a directed gas jet Effect of vacuum on penetration and defects in laser welding Nd:YAG laser welding of titanium alloys using a directed gas jet,” *J. Laser Appl. J. Laser Appl.*, vol. 22, no. 10, pp. 32005–245, 2010.

[76] X. Cao, G. Debaecker, E. Poirier, S. Marya, J. Cuddy, a. Birur, and P. Wanjara, “Tolerances of joint gaps in Nd:YAG laser welded Ti-6Al-4V alloy with the addition of filler wire,” *J. Laser Appl.*, vol. 23, no. 1, p. 012004, 2011.

[77] S. Katayama, Y. Kobayashi, M. Mizutani, and A. Matsunawa, “Effect of vacuum on penetration and defects in laser welding,” *J. Laser Appl.*, vol. 13, no. 5, p. 187, 2001.

[78] F. Caiazzo, F. Curcio, G. Daurelio, F. Memola, and C. Minutolo, “Ti6Al4V sheets lap and butt joints carried out by CO 2 laser: mechanical and morphological characterization,” *J. Mater. Process. Technol.*, vol. 149, pp. 546–552, 2004.

[79] W. W. Duley, *Laser welding*. Wiley, 1999.

[80] X. Cao and M. Jahazi, “Effect of welding speed on butt joint quality of Ti–6Al–4V alloy welded using a high-power Nd:YAG laser,” *Opt. Lasers Eng.*, vol. 47, no. 11, pp. 1231–1241, 2009.

[81] N. K. Babu and S. G. S. Raman, “Influence of current pulsing on microstructure and mechanical properties of Ti–6Al–4V TIG weldments,” *Sci. Technol. Weld. Join.*, vol. 11, no. 4, pp. 442–447, 2006.

[82] S. Sundaresan, G. D. Janaki Ram, and G. Madhusudhan Reddy, “Microstructural refinement of weld fusion zones in α–β titanium alloys using pulsed current welding,” *Mater. Sci. Eng. A*, vol. 262, no. 1–2, pp. 88–100, 1999.

[83] K. K. Murthy, N. B. Potluri, and S. Sundaresan, “Fusion zone microstructure and fatigue crack growth behaviour in Ti-6Al-4V alloy weldments,” *Mater. Sci. Technol.*, vol. 13, no. 6, pp. 503–510, 1997.

[84] J. Oh, N. J. Kim, S. Lee, and E. W. Lee, “Correlation of fatigue properties and microstructure in investment cast Ti-6Al-4V welds,” *Mater. Sci. Eng. A*, vol. 340, pp. 232–242, 2003.

[85] T. Mohandas, M. Srinivas, and V. V. Kutumbarao, “Effect of post-weld heat treatment on fracture toughness and fatigue crack growth behaviour of electron beam welds of a titanium (alpha+beta) alloy,” *Fatigue Fract. Eng. Mater. Struct.*, vol. 23, no. 1, pp. 33–38, 2000.

[86] M. M. Salama, “Fatigue Crack Growth Behavior of Titanium Alloy Ti-6Al-4V and Weldment,” *J. Offshore Mech. Arct. Eng.*, vol. 123, no. 3, p. 141, 2001.

[87] J. Ault, J. Pillers, and S. Veeck, “The GTAW of Ti-6Al-4V castings and its effect on microstructural and mechanical properties,” *Jom*, vol. 57, no. November, pp. 62–65, 2005.

[88] N. E. Dowling, *Mechanical behavior of materials : engineering methods for deformation, fracture, and fatigue*. Pearson/Prentice Hall, 2007.

[89] S. Suresh, *Fatigue of materials*. Cambridge University Press, 1998.

[90] S. J. Maddox, *Fatigue strength of welded structures*. Abington Publishing, 1991.

[91] L. Smith, M. Gittos, and P. Threadgill, “High quality and productivity joining processes and procedures for titanium risers and flowlines,” in *Titanium Risers and Flowlines*, 1999.

[92] S. J. Maddox and S. J., “Recent advances in the fatigue assessment of weld imperfections,” *Weld. J.*, vol. 72, pp. 42–51, 1993.

[93] G. M. Peshak and D. V. Lindh, “The Influence of Weld Defects on Performance,” *Weld. J. (Research Suppl.*, vol. 48, no. 2, pp. 48–56, 1696.

[94] J. Fan, D. L. McDowell, M. F. Horstemeyer, and K. Gall, “Cyclic plasticity at pores and inclusions in cast Al-Si alloys,” *Eng. Fract. Mech.*, vol. 70, pp. 1281–1302, 2003.

[95] Z. Xu, W. Wen, and T. Zhai, “Effects of Pore Position in Depth on Stress/Strain Concentration and Fatigue Crack Initiation,” *Metall. Mater. Trans. A*, vol. 43, no. 8, pp. 2763–2770, Nov. 2011.

[96] S. Tammas-Williams, P. J. Withers, I. Todd, and P. B. Prangnell, “The Influence of Porosity on Fatigue Crack Initiation in Additively Manufactured Titanium Components,” *Sci. Rep.*, vol. 7, no. 1, pp. 1–13, 2017.

[97] Y. Murakami, “Material defects as the basis of fatigue design,” *Int. J. Fatigue*, vol. 41, pp. 2–10, Aug. 2012.

[98] A. Dean, M. Morris, J. Stufken, D. Bingham, *Handbook of Design and Analysis of Experiments*. 2015.

[99] M. J. Harry, *Practitioner’s guide for statistics and lean six sigma for process improvement*. John Wiley & Sons, 2010.

[100] J. I. Goldstein, D. E. Newbury, J. R. Michael, N. W. M. Ritchie, J. H. J. Scott, and D. C. Joy, *Scanning Electron Microscopy and X-Ray Microanalysis*. New York, NY: Springer New York, 2018.

[101] T. Maitland and S. Sitzman, “Electron Backscatter Diffraction (EBSD) Technique and Materials Characterization Examples,” *Scanning Microsc. Nanotechnology. Tech. Appl.*, pp. 41–76, 2007.

[102] T. B. Britton, J. Jiang, Y. Guo, A. Vilalta-Clemente, D. Wallis, L. N. Hansen, A. Winkelmann, and A. J. Wilkinson, “Tutorial: Crystal orientations and EBSD - Or which way is up?,” *Mater. Charact.*, vol. 117, 2016.

[103] L. Germain, N. Gey, and M. Humbert, “Reliability of reconstructed β-orientation maps in titanium alloys,” *Ultramicroscopy*, vol. 107, no. 12, pp. 1129–1135, 2007.

[104] C. Cayron, “ARPGE: A computer program to automatically reconstruct the parent grains from electron backscatter diffraction data,” *J. Appl. Crystallogr.*, vol. 40, no. 6, pp. 1183–1188, 2007.

[105] M. G. Glavicic, P. A. Kobryn, T. R. Bieler, and S. L. Semiatin, "An automated method to determine the orientation of the high-temperature beta phase from measured EBSD data for the low-temperature alpha-phase in Ti-6Al-4V," *Mater. Sci. Eng. A*, vol. 351, no. 1–2, pp. 258–264, 2003.

[106] P. S. Davies, B. P. Wynne, W. M. Rainforth, M. J. Thomas, and P. L. Threadgill, "Development of microstructure and crystallographic texture during stationary shoulder friction stir welding of Ti-6Al-4V," *Metall. Mater. Trans. A Phys. Metall. Mater. Sci.*, vol. 42, no. 8, pp. 2278–2289, 2011.

[107] M. Simonelli, Y. Y. Tse, and C. Tuck, "The formation of α + β microstructure in as-fabricated selective laser melting of Ti–6Al–4V," *J. Mater. Res.*, vol. 29, no. 17, pp. 2028–2035, 2014.

[108] Y. Yang, Y. J. liu, J. Chen, H. L. Wang, Z. Q. Zhang, Y. J. Lu, S. Q. Wu, and J. X. Lin, "Crystallographic features of α variants and β phase for Ti-6Al-4V alloy fabricated by selective laser melting," *Mater. Sci. Eng. A*, vol. 707, no. September, pp. 548–558, 2017.

[109] S. C. Wang, M. Aindow, and M. J. Starink, "Effect of self-accommodation on α/α boundary populations in pure titanium," *Acta Mater.*, vol. 51, no. 9, pp. 2485–2503, 2003.

[110] N. Stanford and P. S. Bate, "Crystallographic variant selection in Ti–6Al–4V," *Acta Mater.*, vol. 52, no. 17, pp. 5215–5224, Oct. 2004.

[111] P. C. Collins, B. Welk, T. Searles, J. Tiley, J. C. Russ, and H. L. Fraser, "Development of methods for the quantification of microstructural features in alpha+beta-processed alpha/beta titanium alloys," *Mater. Sci. Eng. A*, vol. 508, no. 1–2, pp. 174–182, 2009.

[112] J. Tiley, T. Searles, E. Lee, S. Kar, R. Banerjee, J. C. Russ, and H. L. Fraser, "Quantification of microstructural features in alpha/beta titanium alloys," *Mater. Sci. Eng. A*, vol. 372, no. 1–2, pp. 191–198, 2004.

[113] R. Halmshaw, *Industrial Radiology*, vol. 1. Dordrecht: Springer Netherlands, 1995.

[114] J. P. Kruth, M. Bartscher, S. Carmignato, R. Schmitt, L. De Chiffre, and A. Weckenmann, "Computed tomography for dimensional metrology," *CIRP Ann. - Manuf. Technol.*, vol. 60, no. 2, pp. 821–842, 2011.

[115] E. N. Landis and D. T. Keane, "X-ray microtomography," *Mater. Charact.*, vol. 61, no. 12, pp. 1305–1316, 2010.

[116] S. W. Smith, *Digital signal processing : a practical guide for engineers and scientists*. Newnes, 2003.

[117] “Resolution of a 3D X-ray Microscope Defining Meaningful Resolution Parameters for XRM,” 2013.

[118] ASM International, “ASTM E1447-09(2016) Standard Test Method for Determination of Hydrogen in Titanium and Titanium Alloys by Inert Gas Fusion Thermal Conductivity/Infrared Detection Method,” West Conshohocken, PA, 2016.

[119] ASM International, “ASTM E1409-13 Standard Test Method for Determination of Oxygen and Nitrogen in Titanium and Titanium Alloys by Inert Gas Fusion,” West Conshohocken, PA, 2013.

[120] ASM International, “ASTM E1941-10(2016) Standard Test Method for Determination of Carbon in Refractory and Reactive Metals and Their Alloys by Combustion Analysis,” West Conshohocken, PA, 2016.

[121] ASM International, “ASTM E539-11 Standard Test Method for Analysis of Titanium Alloys by X-Ray Fluorescence Spectrometry,” West Conshohocken, PA, 2011.

[122] K. C. W. Yung, B. Ralph, W. Lee, and R. Fenn, “An investigation into welding parameters affecting the tensile properties oftitanium welds,” *J. Mater. Process. Technol.*, vol. 63, no. 96, pp. 759–764, 1997.

[123] H. Okamoto, “B−Ti (Boron-Titanium),” *J. Phase Equilibria Diffus.*, vol. 27, no. 3, pp. 303–303, 2006.

[124] L. Germain, N. Gey, R. Mercier, P. Blaineau, and M. Humbert, “An advanced approach to reconstructing parent orientation maps in the case of approximate orientation relations: Application to steels,” *Acta Mater.*, vol. 60, no. 11, pp. 4551–4562, 2012.

[125] American Welding Society, “Specification for Fusion Welding for Aerospace Applications,” Miami, United States of America, 2001.